



Majorana zero modes in multiplicative topological phasesAdipta Pal ^{1,2}, Joe H. Winter,^{1,2,3} and Ashley M. Cook ^{1,2,*}¹Max Planck Institute for Chemical Physics of Solids, N  thnitzer Strasse 40, 01187 Dresden, Germany²Max Planck Institute for the Physics of Complex Systems, N  thnitzer Strasse 38, 01187 Dresden, Germany³SUPA, School of Physics and Astronomy, University of St. Andrews, North Haugh, St. Andrews KY16 9SS, United Kingdom

(Received 24 February 2023; revised 28 November 2023; accepted 7 December 2023; published 18 January 2024)

Topological qubits composed of unpaired Majorana zero modes are under intense experimental and theoretical scrutiny in efforts to realize practical quantum computation schemes. In this work, we show that the minimum four *unpaired* Majorana zero modes required for a topological qubit according to braiding schemes and control of entanglement for gate operations are inherent to multiplicative topological phases, which realize symmetry-protected tensor products—and maximally entangled Bell states—of unpaired Majorana zero modes. We construct and characterize both one-dimensional and two-dimensional multiplicative topological phases with two parent Kitaev chain Hamiltonians. We furthermore characterize topology in the bulk and on the boundary with established methods while also introducing techniques to overcome challenges in characterizing multiplicative topology. In the process, we explore the potential of these multiplicative topological phases for an alternative to braiding-based topological quantum computation schemes, in which gate operations are performed through topological phase transitions.

DOI: [10.1103/PhysRevB.109.014516](https://doi.org/10.1103/PhysRevB.109.014516)**I. INTRODUCTION**

Topological quantum computation schemes are central to the study of topological condensed matter, and they are viewed as one of their most important and practical applications. In particular, they hold great promise for overcoming challenges of decoherence associated with scalable quantum computation schemes [1]. These schemes rely upon the realization of topological qubits consisting of quasiparticles with non-Abelian exchange statistics, with the simplest and most widely studied of these quasiparticles being the unpaired Majorana zero mode (MZM) [2–4]. This area of research has expanded rapidly in the past two decades, with many recent experimental works reporting signatures associated with unpaired Majorana zero modes [5,6], along with a tremendous number of theoretical proposals for experimental realization and practical application [7,8].

To construct a topological qubit from unpaired Majorana zero modes, *two pairs* of unpaired Majorana zero modes are required at minimum by proposals based on braiding [9,10], and some gate operations required for topological quantum computation utilize controlled entanglement [11]. The recently introduced multiplicative topological phases (MTPs) [12]—topological phases of matter corresponding

to a symmetry-protected tensor product structure in which multiple parent topological phases may be combined in a multiplicative fashion to realize novel topology—present an opportunity to elegantly meet these requirements. If two parent topological phases, each realizing unpaired Majorana zero modes, are combined in this manner, states consisting of tensor products of unpaired Majorana zero modes are possible. As shown in work introducing MTPs [12], it is furthermore possible to selectively entangle topologically protected boundary modes while respecting symmetries protecting the multiplicative topological phase in the bulk, which could potentially be used to introduce entanglement in a controlled manner for the purpose of gate operations.

For these reasons, we introduce multiplicative topological phases constructed from parent phases realizing unpaired Majorana zero modes in this work. We choose parent Hamiltonians to be instances of the canonical Kitaev chain model [13]. We find that, for the models considered, these MZMs realize a variety of two-qubit states in different regions of the phase diagram. This indicates that these MZMs have the potential to serve as an alternative platform for topological quantum computation to braiding schemes, in which each parent of the multiplicative phase provides a qubit, and the minimum number of MZMs for a qubit is instead effectively two.

We also explore the potential of multiplicative topology to realize novel physics in this work of interest beyond quantum computation schemes: while the Kitaev chain realizes a one-dimensional topological phase, a multiplicative topological phase constructed from two parent Kitaev chains can actually be one-dimensional or two-dimensional. We consider both constructions in this work using Kitaev chain parent phases, realizing one-dimensional and two-dimensional multiplicative Kitaev chain (MKC) constructions, and studying

*Corresponding author: cooka@pks.mpg.de

the multiplicative Majorana zero modes resulting in each case. To characterize the arising multiplicative phases, we study the Wannier center spectrum of the MKC, and we find that its eigenvalues are sums of the eigenvalues of the parent Wannier center spectra. As a result, Wilson loops can fail to characterize multiplicative topology in certain cases. We show, however, that the MKC can be decomposed into parts, and winding numbers for these components can be used to characterize topological phases realized by the MKC.

We begin by first reviewing the Kitaev chain and its topological classification in Sec. II. In Sec. III we introduce a one-dimensional MKC and present its spectrum and bound states. Finally, in Sec. IV we introduce a two-dimensional MKC, also characterizing its spectral properties and bulk-boundary correspondence.

II. PARENT HAMILTONIANS

To realize topologically protected states analogous to unpaired Majorana zero modes in multiplicative topological phases, we construct them from two parent Hamiltonians. The latter are described by a Hamiltonian core to many leading experimental proposals [3,14–19] for realization of unpaired Majorana zero modes and topological qubits known as the Kitaev chain [20,21]. Given the foundational nature of the Kitaev chain in topological quantum computation [4,13], our results are broadly relevant to the study of quasiparticles in multiplicative phases relevant to topological quantum computation. We further show that phases in which multiplicative Majorana zero modes are realized exhibit a number of unique features of considerable fundamental interest in the study of topological phases of matter, and they are promising for topological quantum computation schemes.

First, we review the Kitaev chain model and its significance to platforms for topological quantum computation. The one-dimensional Kitaev chain model is a foundational tight-binding model describing spinless complex fermions hopping between nearest-neighbor sites, with additional $p + ip$ superconducting pairing [20]. More specifically, the real-space Hamiltonian for the Kitaev chain (KC) takes the form [13]

$$H_{\text{KC}} = - \sum_{j=1}^N \mu c_j^\dagger c_j - \sum_{j=1}^{N-1} t (c_j^\dagger c_{j+1} + \text{H.c.}) + \sum_{j=1}^{N-1} \Delta (c_j c_{j+1} + \text{H.c.}), \quad (1)$$

where here c_j^\dagger creates an electron at site j , μ is the chemical potential, t is the nearest-neighbor hopping integral, and Δ is the superconducting pairing strength.

The fermion number parity conservation of the superconductor yields two sectors of the Hilbert space, one with even ground-state parity and one with odd ground-state parity [13]. For odd parity and open boundary conditions (OBCs) for the chain, the ground-state manifold is degenerate and composed of states strongly localized at its ends. Within the ground-state manifold, furthermore, states may be constructed with wave functions strongly localized at only one end of the chain or the other, which are of Majorana character [13]. These

two Majorana bound states constitute a physical fermion that allows information to be encoded nonlocally, providing a robust platform for quantum computing.

The single-particle sector of the model also displays the desired unpaired Majorana zero modes at the ends of the chain for open boundary conditions, and it is widely studied and experimentally relevant [22]. This version is sufficient for the purpose of introducing multiplicative topological phases based upon the Kitaev chain, and we restrict ourselves to this case for the remainder of the manuscript.

We first consider the infinitely long chain in the single-particle regime with periodic boundary conditions. Fourier-transforming the Hamiltonian and imposing particle-hole symmetry (PHS) through a redundancy, we express the model in terms of a Bogoliubov–de Gennes Hamiltonian $H_{\text{BdG}}(k)$,

$$H_{\text{KC}} = \frac{1}{2} \sum_k \Psi_k^\dagger H_{\text{BdG}}(k) \Psi_k, \quad (2)$$

$$H_{\text{BdG}}(k) = - (2t \cos k + \mu) \tau^z + 2\Delta \sin k \tau^y. \quad (3)$$

Here, $\Psi_k = (c_k, c_{-k}^\dagger)^T$, with c_k annihilating a complex, spinless fermion with momentum k , reflecting the particle-hole degree of freedom incorporated explicitly into the Hamiltonian, and τ^j , where $j \in \{x, y, z\}$ is a Pauli matrix.

For this effectively mean-field description of a superconductor, the Bloch Hamiltonian may be diagonalized to compute the bulk spectrum as $\epsilon_\pm(k) = \pm \sqrt{(2t \cos k + \mu)^2 + 4\Delta^2 \sin^2 k}$. From this expression, we see that the Bloch Hamiltonian is gapped for $|\mu| < 2t$ and $|\mu| > 2t$, with gap closings occurring at $k = \pi$ ($k = 0$) for $\mu = 2t$ ($\mu = -2t$). A topologically nontrivial phase is realized in the former regime, which may be characterized in the bulk by various methods [23] as well as explicit verification of unpaired Majorana zero modes. The latter is facilitated by considering the Majorana representation of the finite Kitaev chain [13]. For now, we consider the latter and express the BdG Hamiltonian in terms of Majorana operators with the convention $c_j = \frac{1}{2}(\gamma_{j,+} + i\gamma_{j,-})$, where $\{\gamma_\alpha, \gamma_\beta\} = 2\delta_{\alpha\beta}$ and $\gamma_\alpha^\dagger = \gamma_\alpha$, yielding the following expression for the Hamiltonian:

$$H_{\text{KC}} = - \sum_{j=1}^N \frac{\mu}{2} (1 + i\gamma_{j,+}\gamma_{j,-}) - \sum_{j=1}^{N-1} \frac{t}{2} (i\gamma_{j,+}\gamma_{j+1,-} + i\gamma_{j+1,+}\gamma_{j,-}) + \sum_{j=1}^{N-1} \frac{\Delta}{2} (i\gamma_{j,+}\gamma_{j+1,-} - i\gamma_{j+1,+}\gamma_{j,-}). \quad (4)$$

Notice that for $t = \Delta$ and $\mu = 0$, we have $[H_{\text{KC}}, \gamma_{1,-}] = [H_{\text{KC}}, \gamma_{N,+}] = 0$, which implies we have two Majorana zero modes, each with zero energy and localized at one end of the chain.

We will now construct multiplicative topological phases (MTPs) with two parent Kitaev chain Hamiltonians $H_{p,1}(k_i)$ and $H_{p,2}(k_j)$, where k_i and k_j are momenta in directions i and j . We take i and j to either be parallel (i and j are each taken to be x , and $k_i = k_j = k_x$ corresponds to momentum in

the x direction, for instance) or perpendicular [i and j are taken to be x and y , for instance, with $H_{p,1}(k_x)$ describing a Kitaev chain parallel to the x -axis and $H_{p,2}(k_y)$ describing a Kitaev chain parallel to the y -axis in the x - y plane]. In this way, we may realize multiplicative topological phases that are either one-dimensional ($i = j$) or two-dimensional ($i \neq j$). We express parent Hamiltonian α (with $\alpha \in \{1, 2\}$) using a vector of momentum-dependent parameters $\mathbf{d}(k)_\alpha = (d(k)_{1\alpha}, d(k)_{2\alpha}, d(k)_{3\alpha})$ dotted into a vector of Pauli matrices $\boldsymbol{\tau} = (\tau_x, \tau_y, \tau_z)$ for parent 1 and $\boldsymbol{\sigma} = (\sigma_x, \sigma_y, \sigma_z)$ for parent 2, as

$$H_{p,1}(k_i) = \mathbf{d}(k_i)_1 \cdot \boldsymbol{\tau}, \quad (5a)$$

$$H_{p,2}(k_j) = \mathbf{d}(k_j)_2 \cdot \boldsymbol{\sigma}. \quad (5b)$$

The child Hamiltonian is then compactly expressed in terms of the parent Hamiltonians using the concrete derivation of the exceptional isomorphism $\text{SO}(4) \cong \text{SU}(2) \times \text{SU}(2)/\mathbb{Z}_2$ provided in Cook and Moore [12], as

$$H_{12}^c(\mathbf{k}) = \mathbf{d}(k_i)_1 \cdot \boldsymbol{\tau} \otimes (-d(k_j)_{12}, d(k_j)_{22}, -d(k_j)_{32}) \cdot \boldsymbol{\sigma}, \quad (6)$$

and the momentum vector $\mathbf{k} = k_i \hat{i} + k_j \hat{j}$ being simply $\mathbf{k} = k_i \hat{i}$ for $i = j$. Alternative combinations of the parent Hamiltonians in tensor product constructions also yield child Hamiltonians, including $H_{12}^c(\mathbf{k}) = H_{p,1}(k_i) \otimes H_{p,2}(k_j)$. The tensor product structure is protected by a combination of symmetries enforced on the child Hamiltonian and symmetries enforced on the parent Hamiltonians as discussed by Cook and Moore [12]. This results in the child Hamiltonian possessing the following symmetries according to standard analysis purely at the level of child [24,25]:

$$\mathcal{T} = \mathcal{K}, \quad (7a)$$

$$\mathcal{P}_1 = \mathcal{I} \otimes \sigma^x \mathcal{K}, \quad (7b)$$

$$\mathcal{C}_1 = \mathcal{I} \otimes \sigma^x, \quad (7c)$$

$$\mathcal{P}_2 = \tau^x \mathcal{K} \otimes \mathcal{I}, \quad (7d)$$

$$\mathcal{C}_2 = \tau^x \otimes \mathcal{I}, \quad (7e)$$

where \mathcal{T} , \mathcal{P} , and \mathcal{C} correspond to time-reversal, particle-hole, and chiral symmetry, respectively. In addition to the discrete symmetries, the child multiplicative Kitaev chain has a *unitary symmetry*, given by $\mathcal{U} = \tau^x \sigma^x$. Such a unitary symmetry naturally emerges in the child Hamiltonian by its tensor product form in terms of the parent Hamiltonians and each parent possessing chiral symmetry. This permits block diagonalization of the child Hamiltonian, as we show in this work. This motivates further development of methods for symmetry analysis, as such analysis at the level of the child and parents in combination rather than strictly at the level of the child reveals different information about the system that is useful in characterizing topological systems given the possibility of multiplicative topology.

We comment briefly on the interpretation of the basis for the child Hamiltonian, as there are two possible options. One possibility is to interpret the resultant Hamiltonian as quadratic, describing an effectively noninteracting system. However, we may also interpret the bases of the child Hamiltonians discussed here as tensor products of single-particle bases of the parents, corresponding to a basis for the child that

is purely quartic. In this second interpretation, therefore, the Hamiltonian characterizes a strongly correlated system. We focus on the first interpretation in this work, and we will explore the second interpretation in greater detail in later work.

III. CHILD HAMILTONIAN FOR PARALLEL PARENT CHAINS

We first consider the MKC for two parallel parent Kitaev chains, corresponding to $i = j$ above. We therefore take $k_i = k_j = k$ to simplify notation. The parent and child Hamiltonians then take the following forms:

$$H_{\text{KC},1}(k) = -(2t_1 \cos k + \mu_1)\tau^z + 2\Delta_1 \sin k \tau^y,$$

$$H_{\text{KC},2}(k) = -(2t_2 \cos k + \mu_2)\sigma^z + 2\Delta_2 \sin k \sigma^y,$$

$$H_{\text{MKC},\parallel}^c(k) = [-(2t_1 \cos k + \mu_1)\tau^z + 2\Delta_1 \sin k \tau^y] \otimes [(2t_2 \cos k + \mu_2)\sigma^z + 2\Delta_2 \sin k \sigma^y]. \quad (8)$$

We characterize the MKC in this case first by studying the bulk spectrum and then by studying bulk boundary correspondence analytically and numerically.

A. Bulk properties of the parallel MKC

In this subsection, we investigate the bulk properties of the parallel multiplicative Kitaev chain. First, we start with the properties of the bulk spectrum and then study the model's topological attributes.

1. Bulk spectrum of the parallel MKC

The spectrum of the child Hamiltonian $H_{\text{MKC},\parallel}^c(k)$ consists of doubly degenerate eigenvalues given by

$$E(k) = \pm \sqrt{[2t_1 \cos(k) + \mu_1]^2 + [2\Delta_1 \sin(k)]^2} \times \sqrt{[2t_2 \cos(k) + \mu_2]^2 + [2\Delta_2 \sin(k)]^2}. \quad (9)$$

This corresponds to the bulk gap closing under the following conditions:

$$\mu_{1,2} = \begin{cases} -2t_{1,2} & \text{if } k = 0, \\ +2t_{1,2} & \text{if } k = \pi, \\ -2 \cos(k)t_{1,2} & \text{if } \Delta_{1,2} = 0. \end{cases} \quad (10)$$

We illustrate these in Fig. 1, where we show the MKC spectrum as a function of k for a set of representative points in a phase diagram generated by fixing $t_1 = t_2 = 1$ and varying μ_1 and μ_2 . Figures 1(a)–1(d) show that the bulk gap closing points are inherited from the parents, as the eigenvalues of the MKC correspond to the product of two Kitaev chains eigenvalues for different configurations.

2. Quasiparticle velocities near critical points

For the case of the parallel MKC, we examine the Dirac Hamiltonians near each of the gapless points. For both $\mu_1 \sim -2t_1$ and $\mu_2 \sim -2t_2$, the gap closes for $k = 0$, so that we get the following Dirac Hamiltonian in its vicinity:

$$H_{\text{Dirac}}^c(k) = -(2t_1 + \mu_1)(2t_2 + \mu_2)\Gamma^{zz} + 2\Delta_1(2t_2 + \mu_2)k\Gamma^{yz} - 2\Delta_2(2t_1 + \mu_1)k\Gamma^{xy}, \quad (11)$$

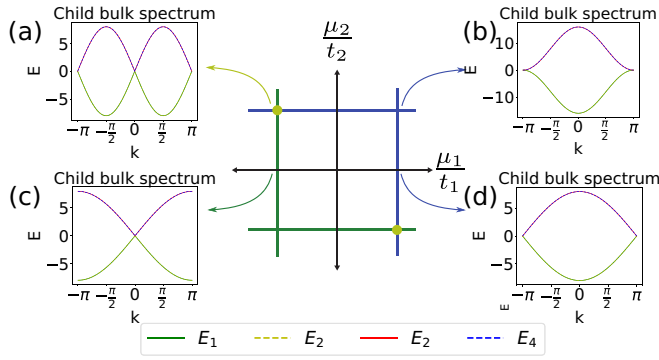


FIG. 1. Dependence of the bulk dispersion of the child Hamiltonian $H_{\text{MKC},||}^c(k)$ in Eq. (8) on parameters of its parent Hamiltonians $H_{\text{KC},1}(k)$ and $H_{\text{KC},2}(k)$. Example bulk dispersions for $H_{\text{MKC},||}^c(k)$ are shown in (a), (b), (c), and (d) for parameter values $(\frac{\mu_1}{t_1}, \frac{\mu_2}{t_2}) = (-2, 2), (2, 2), (-2, 0),$ and $(2, 0)$, respectively. The child bulk gap closes at $k = 0$ along the green line, at $k = \pi$ along the blue line, and at $k = 0, \pi$ on the yellow dots, in agreement with Eq. (10) for $\Delta_1 \neq 0, \Delta_2 \neq 0$.

where $\Gamma^{ij} = \tau^i \sigma^j$. Denote $m_j = 2t_j + \mu_j$ ($j = 1, 2$). The energies are doubly degenerate and given as

$$E(k) = \pm \sqrt{4(\Delta_2 m_1 - \Delta_1 m_2)^2 k^2 + m_1^2 m_2^2}. \quad (12)$$

Notice, for the gapless point $\mu_1 = -2t_1$, or $m_1 = 0$, that the energy expression can be simplified as $E(k) = \pm 2\Delta_1 m_2 k$, and similarly for the gapless point $\mu_2 = -2t_2$, or $m_2 = 0$, the expression becomes $E(k) = \pm 2\Delta_2 m_1 k$. It is important to note that when $m_1 = 0 = m_2$ simultaneously, a quadratic expansion is required to capture the low-energy dispersion, which yields

$$H_2^c(k) = -[m_1 m_2 - (t_1 m_2 + t_2 m_1) k^2] \Gamma^{zz} + 2\Delta_1 m_2 k \Gamma^{zy} - 2\Delta_2 m_1 k \Gamma^{zy} + \Delta_1 \Delta_2 k^2 \Gamma^{yy}. \quad (13)$$

Denoting $t_1 m_2 + t_2 m_1 = M$, the spectrum is given by the four eigenvalues

$$E(k) = \pm [(M \mp \Delta_1 \Delta_2) k^2 - m_1 m_2]^2 + 4k^2 (\Delta_2 m_1 \mp \Delta_1 m_2)^2 k^2]^{\frac{1}{2}}. \quad (14)$$

As stated, for the case, $m_1 = m_2 = 0$, the dispersion relation $E = \pm \Delta_1 \Delta_2 k^2$ is quadratic and doubly degenerate.

3. Bulk topology of the parallel MKC

While the computation of bulk topological invariants for the parent Kitaev chains is known, this is not the case for the topological invariants of the MKC. Although the topology of multiplicative phases can be understood in terms of their parents' topological invariants, the methods for characterizing these Hamiltonians, without knowledge of their decomposition into parent Hamiltonians, have not been established.

One of the more robust methods for characterizing topology is the analysis of the Wilson loop spectrum. The Wilson loop [26] is a unitary operator defined over a closed path as

$$\mathcal{W} = \overline{\text{exp}} \left[i \int_{\text{BZ}} d\mathbf{k} \cdot \mathbf{A}(\mathbf{k}) \right], \quad (15)$$

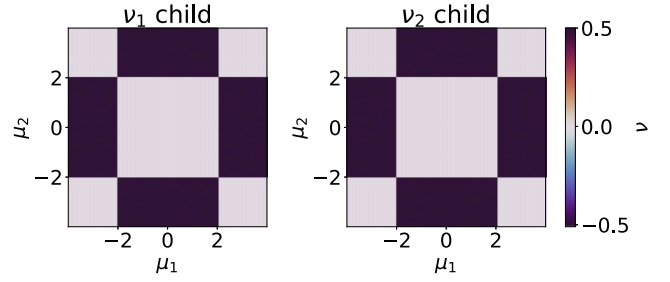


FIG. 2. Wannier centers for a child Hamiltonian at half-filling with parents with parameters $t_1 = t_2$ and $\Delta_1 = \Delta_2$. These correspond to the Wilson loop eigenvalues after integrating along k_x .

where \mathbf{A} is the non-Abelian Berry connection:

$$A_{mn}(\mathbf{k}) = i \langle u_m(\mathbf{k}) | \nabla_{\mathbf{k}} | u_n(\mathbf{k}) \rangle. \quad (16)$$

Here $|u_n(\mathbf{k})\rangle$ are Bloch states in the occupied subspace, and \mathbf{A} is defined a Hermitian operator. Consequently, \mathcal{W} is a unitary operator whose eigenvalues are $e^{i2\pi \nu_j}$, where ν_j are the Wannier centers of charge.

We compute the Wannier centers for topologically distinct regions of the phase diagram determined by the topological invariants of the parents. Each parent Hamiltonian has a \mathbb{Z}_2 topological classification, so the child Hamiltonian has a $\mathbb{Z}_2 \times \mathbb{Z}_2$ classification, with its invariant ν_C expressed in terms of the parent invariants $\nu^{(1)}$ and $\nu^{(2)}$ as $\nu_C = (\nu^{(1)}, \nu^{(2)})$, where $\nu^{(1,2)} \in \{0, 0.5\} \pmod{1}$ indicates the topological phase of each parent.

In the trivial phase, the Wannier center of the occupied band is located at the center ($\nu = 0$) of the unit cell, and at the edge ($\nu = 0.5$) in the topological phase. Therefore, we calculate for the MKC parallel case, where we have a single-momentum component, and find that the two eigenvalues indicate a shift of the Wannier centers to the edge when only one of the parent phases is topological but not both. This inability of the Wilson loop method to detect some multiplicative phases results from the multiplicative dependence of the child Wilson loop on the Wilson loops of the parents.

The Wannier centers of charge of the MKC at half-filling ($M = 2$ is the number of occupied orbitals) are shown in Fig. 2. The doubly degenerate occupied states correspond to two equivalent Wannier centers ν_1 and ν_2 , as shown by Figs. 2(a) and 2(b). Unexpectedly, both an MKC with $|\mu_1| = |\mu_2| < 2$ and an MKC with $|\mu_1| = |\mu_2| > 2$ have the Wannier centers localized at the center of the unit cell ($\nu_1 = \nu_2 = 0$), despite the fact that finite chains with the former set of parameters have bound states, while finite chains with the latter set of parameters do not. It is only for parent Hamiltonians of different topology that the Wannier centers of a half-filled MKC localize at the edge ($\nu_1 = \nu_2 = 0.5$), showing that the MKC Wilson loop eigenvalues correspond to the ones given by the parents' Wannier centers. This is analytically shown in Appendix S2 of the Supplemental Material [27].

However, we have observed that the MKC possesses three defining symmetries, namely two chiral symmetries inherited from its parents— $\tau^x \otimes \mathcal{I}$ and $\mathcal{I} \otimes \sigma^x$ —and the unitary symmetry generated from their product, $\tau^x \otimes \sigma^x$. We are able to block-diagonalize the parallel MKC Bloch Hamiltonian

via the diagonal basis of the unitary symmetry. The resulting two-band blocks of the four-band Hamiltonian are then called component Hamiltonians. These component Hamiltonians look like the generic two-band Kitaev chains but with next-nearest-neighbor coupling. The resulting component Hamiltonians are defined as follows:

$$H_{\text{MKC},\parallel}^c = \frac{1}{2} \sum_k \tilde{\mathbf{c}}_{k,1}^\dagger \mathcal{H}_{\parallel,1}(k) \tilde{\mathbf{c}}_{k,1} + \frac{1}{2} \sum_k \tilde{\mathbf{c}}_{k,2}^\dagger \mathcal{H}_{\parallel,2}(k) \tilde{\mathbf{c}}_{k,2},$$

$$(\tilde{\mathbf{c}}_{k,1}, \tilde{\mathbf{c}}_{k,2})^T = U^\dagger (c_{k,\uparrow}, c_{k,\downarrow}, c_{-k,\uparrow}^\dagger, c_{-k,\downarrow}^\dagger)^T, \quad (17)$$

where

$$\tilde{c}_{k,1} = (\tilde{c}_{k,\uparrow}, \tilde{c}_{-k,\downarrow}^\dagger)^T, \quad \tilde{c}_{k,2} = (\tilde{c}_{k,\downarrow}, \tilde{c}_{-k,\uparrow}^\dagger)^T,$$

$$U = \frac{1}{\sqrt{2}} \begin{pmatrix} 1 & 0 & 0 & 1 \\ 0 & 1 & 1 & 0 \\ 0 & 1 & -1 & 0 \\ 1 & 0 & 0 & -1 \end{pmatrix},$$

$$\begin{aligned} \mathcal{H}_{\parallel,1}(k) = & -[2(\mu_1 t_2 + \mu_2 t_1) \cos k + 2(t_1 t_2 + \Delta_1 \Delta_2) \cos 2k \\ & + \mu_1 \mu_2 + 2t_1 t_2 - 2\Delta_1 \Delta_2] \sigma^z \\ & + [2(\mu_2 \Delta_1 + \mu_1 \Delta_2) \sin k \\ & + 2(t_2 \Delta_1 + t_1 \Delta_2) \sin 2k] \sigma^y = \mathbf{d}_1(k) \cdot \boldsymbol{\sigma}, \quad (18a) \end{aligned}$$

$$\begin{aligned} \mathcal{H}_{\parallel,2}(k) = & -[2(\mu_1 t_2 + \mu_2 t_1) \cos k + 2(t_1 t_2 - \Delta_1 \Delta_2) \cos 2k \\ & + \mu_1 \mu_2 + 2t_1 t_2 + 2\Delta_1 \Delta_2] \sigma^z \\ & + [2(\mu_2 \Delta_1 - \mu_1 \Delta_2) \sin k \\ & + 2(t_2 \Delta_1 - t_1 \Delta_2) \sin 2k] \sigma^y = \mathbf{d}_2(k) \cdot \boldsymbol{\sigma}, \quad (18b) \end{aligned}$$

Here, each of the component Hamiltonians Eqs. (18a) and (18b) results in the nondegenerate energy dispersion $E(k)$ from Eq. (9), which is equivalent to the MKC parallel dispersion.

Next, we study the winding number for the two component Bloch Hamiltonians by constructing the parametric curves $\mathbf{d}_1(k)$ and $\mathbf{d}_2(k)$ from Eqs. (18a) and (18b) when k is varied in the interval $[0, 2\pi)$. For each of the parent Kitaev chains, the system is said to be in the topological phase with winding number $\mathcal{W} = \pm 1$ if the parametric curve winds around the origin once. At the critical point, the parametric curve intersects the origin, while in the trivial phase it does not wind around the origin at all. Based on similar views, we try to infer the parametric curves due to our component Hamiltonians.

From Figs. 3(a) and 3(b), we observe that for $t_1 = t_2 = 1 = \Delta_1 = \Delta_2$, when both parent KCs are topological, i.e., $\mu_i < 2t_i$, $i \in \{1, 2\}$, the curve due to $\mathbf{d}_1(k)$ winds around the origin twice while the curve from $\mathbf{d}_2(k)$ does not wind around the origin at all, giving rise to an overall winding number, $\mathcal{W} = 2$. We also check all three critical points—when either one of the parents is critical or both of them are, in which case both the parametric curves intersect the origin, albeit in different configurations. For example, Figs. 3(c) and 3(d) show the case when one parent is topological while the other is critical. Finally, we consider the case in which one parent is topological while the other is trivial ($\mu_1 < 2t_1$ and $\mu_2 > 2t_2$ or *vice versa*). The winding for each component Hamiltonian in this case is shown in Figs. 3(e) and 3(f). We see that both curves derived from $\mathbf{d}_1(k)$ and $\mathbf{d}_2(k)$ each wind around the

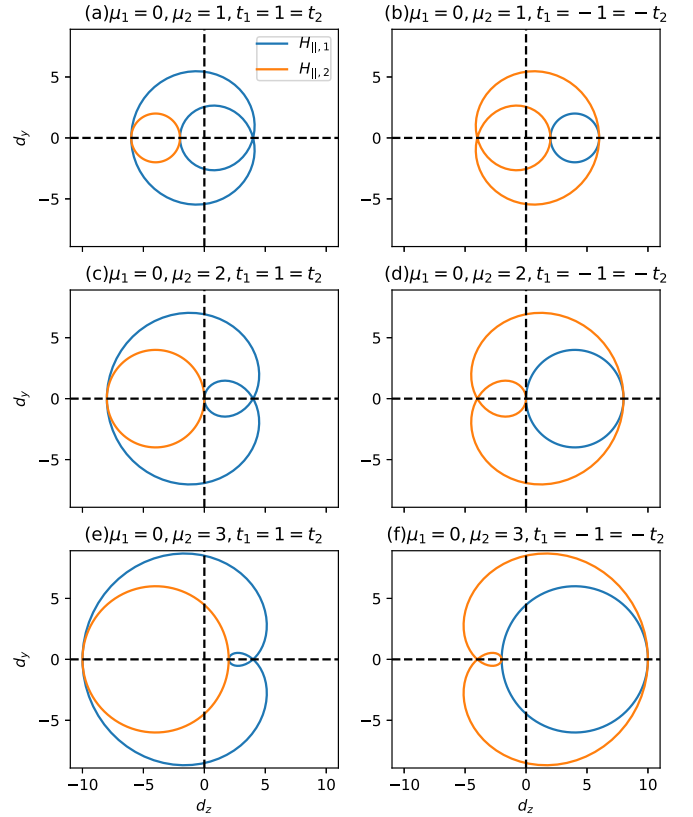


FIG. 3. Parametric curves $\mathbf{d}_1(k)$ and $\mathbf{d}_2(k)$ for the Hamiltonian components $H_{\parallel,1}$ (blue) and $H_{\parallel,2}$ (orange), respectively, as k is varied in the interval $[0, 2\pi)$. The winding of the curves around the origin shows the different topological characteristics for different values of μ_2 with $\mu_1 = 0$ for the cases $t_1 = 1 = t_2$ [first column, (a), (c), and (e)] and $t_1 = -1 = t_2$ [second column, (b), (d), and (f)] at $\Delta_1 = \Delta_2 = 1$ for all cases.

origin once, giving rise to the winding number $\mathcal{W} = 1 \oplus 1$. The origin of these winding numbers can be linked to the two chiral symmetries of the Bloch Hamiltonian. The basis that results in the block diagonalization can also be seen as performing a chiral decomposition in each parent and taking their tensor product. The resulting blocks therefore contain the winding integrand from each parent, and thus the winding number of each component Hamiltonian is formed from these integrands.

Ultimately, the bulk topology can be linked to a rich edge phenomenology in the form of multiplicative unpaired Majoranas. These novel states will be analyzed in the following section, and importantly we will demonstrate their utility in quantum information.

B. Parallel MKC Hamiltonian in real space

The lattice Hamiltonian in the Majorana representation shows the different phases of the Kitaev chain as well as the MKC rewritten in terms of different SSH models. We utilize a diagrammatic approach in Fig. 4 to provide a clear description about the position of the Majorana zero modes and also an analytical explanation of the features we have shown numerically.

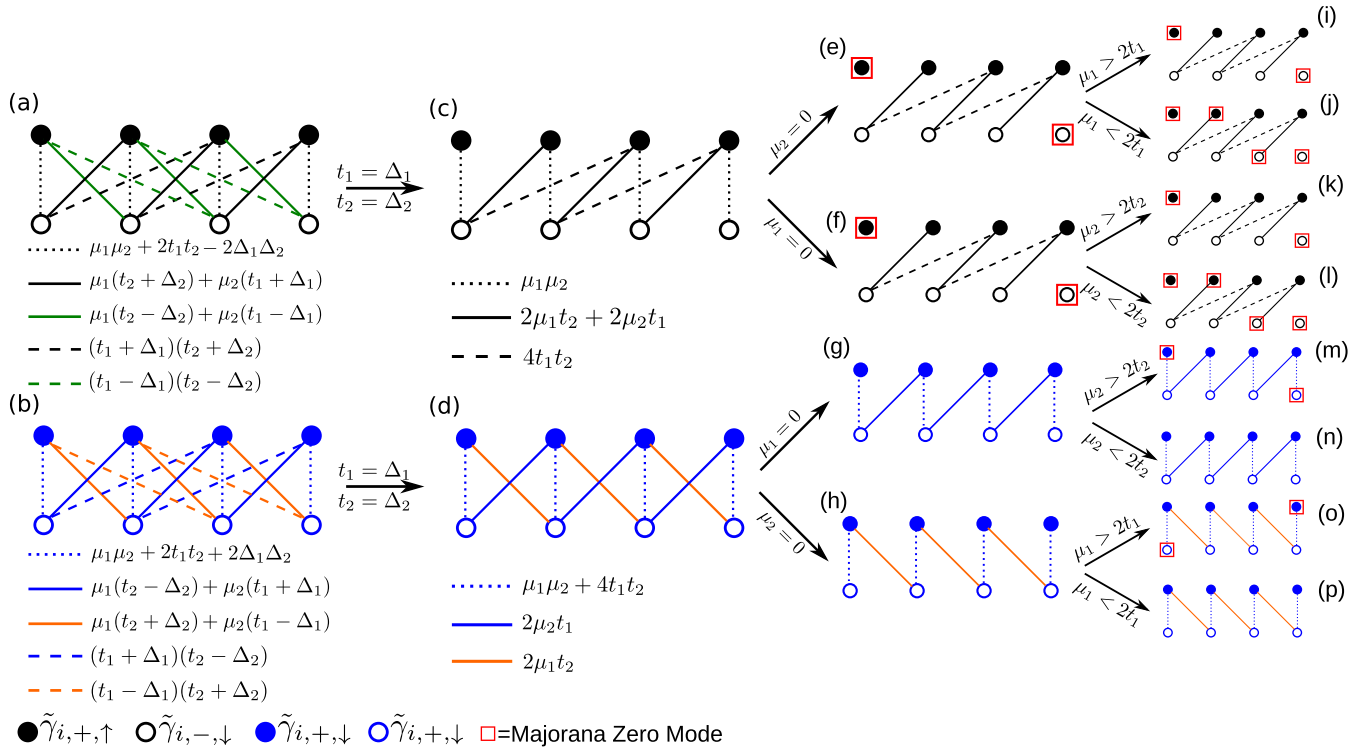


FIG. 4. MKC parallel Hamiltonian in the Majorana basis. The exact Majorana zero modes for the cases in which one parent is topological and the other trivial, and the case in which both parents are topological, are shown schematically. The two Hamiltonians $H_{1,||}$ and $H_{2,||}$ are represented in separate color schemes in (a) and (b), respectively, as shown in the adjoining legends. Parts (c) and (d) refer to the modified system when one imposes the condition $t_i = \Delta_i$ ($i = \{1, 2\}$). Parts (f) and (g) show the respective systems when the first parent is topological with $\mu_1 = 0$. Parts (e) and (h) show the respective systems when the second parent is topological with $\mu_2 = 0$. The last column shows different outcomes for the positions of Majorana zero modes when either only one parent is topological or both of them are topological. The (red) square indicates the position of the Majorana zero mode.

We expect that the MKC has unpaired Majorana bound states in even quantities from winding number calculations. We use this fact to analytically characterize the MKC by defining pseudospinful Majoranas via the following expression: $c_{j,\sigma} = \frac{1}{2}(\gamma_{j,+,\sigma} + i\gamma_{j,-,\sigma})$. We may then, for a given lattice

site, group two such Majoranas with opposite pseudospins into the two-component vectors, $\gamma_{j,+} = (\gamma_{j,+,\uparrow}, \gamma_{j,+,\downarrow})$ and $\gamma_{j,-} = (\gamma_{j,-,\uparrow}, \gamma_{j,-,\downarrow})^T$, so that we can visualize any analysis of the possible phases. The MKC parallel Hamiltonian is then shown as follows:

$$\begin{aligned}
 H_{\text{MKC},||}^c = & \frac{i}{2} \sum_j -\gamma_{j,+} [(\mu_1\mu_2 + 2t_1t_2)\sigma^z - 2i\Delta_1\Delta_2\sigma^y] \gamma_{j,-} - \gamma_{j,+} \{[(t_2\mu_1 + t_1\mu_2) - \mu_2\Delta_1]\sigma^z - i\mu_1\Delta_2\sigma^y\} \gamma_{j+1,-} \\
 & - \gamma_{j+1,+} \{[(t_2\mu_1 + t_1\mu_2) + \mu_2\Delta_1]\sigma^z + i\mu_1\Delta_2\sigma^y\} \gamma_{j,-} - (t_1 - \Delta_1)\gamma_{j,+}(t_2\sigma^z - i\Delta_2\sigma^y)\gamma_{j+2,-} \\
 & - (t_1 + \Delta_1)\gamma_{j+2,+}(t_2\sigma^z + i\Delta_2\sigma^y)\gamma_{j,-}.
 \end{aligned} \tag{19}$$

In this form, three kinds of interaction terms are distinguishable, namely the on-site interaction, the nearest-neighbor interaction, and the next-nearest-neighbor interaction. The matrix structure of the coefficients implies the presence of inter-pseudospin interactions.

To visualize the Majorana bound states, we perform a similarity transformation, $h \rightarrow \mathcal{U}h\mathcal{U}^\dagger$, $\gamma_{j,+} \rightarrow \tilde{\gamma}_{j,+} = \gamma_{j,+}\mathcal{U}^\dagger$, and $\gamma_{j,-} \rightarrow \tilde{\gamma}_{j,-} = \mathcal{U}\gamma_{j,-}$, where, $\mathcal{U} = \frac{1}{\sqrt{2}}(\sigma^0 - i\sigma^y)$, after which the two components of $\tilde{\gamma}_{j,\pm}$ still satisfy the Majorana anticommutation relations, $\{\tilde{\gamma}_j, \tilde{\gamma}_k\} = 2\delta_{jk}$. The transformation \mathcal{U} changes σ^z to σ^x , so that the resulting Hamiltonian is off-diagonal and separates it into two separate inter-pseudospin coupling parts,

$$\begin{aligned}
 H_{\text{MKC},||}^c = & \frac{i}{2} \sum_j \{ -(\mu_1\mu_2 + 2t_1t_2 - 2\Delta_1\Delta_2)\tilde{\gamma}_{j,\uparrow,+}\tilde{\gamma}_{j,\downarrow,-} - [\mu_1(t_2 - \Delta_2) + \mu_2(t_1 - \Delta_1)]\tilde{\gamma}_{j,\uparrow,+}\tilde{\gamma}_{j+1,\downarrow,-} \\
 & - [\mu_1(t_2 + \Delta_2) + \mu_2(t_1 + \Delta_1)]\tilde{\gamma}_{j+1,\uparrow,+}\tilde{\gamma}_{j,\downarrow,-} - (t_1 - \Delta_1)(t_2 - \Delta_2)\tilde{\gamma}_{j,\uparrow,+}\tilde{\gamma}_{j+2,\downarrow,-}
 \end{aligned}$$

$$\begin{aligned}
& - (t_1 + \Delta_1)(t_2 + \Delta_2)\tilde{\gamma}_{j+2,\uparrow,+}\tilde{\gamma}_{j,\downarrow,-} + \frac{i}{2} \sum_j \{ -(\mu_1\mu_2 + 2t_1t_2 + 2\Delta_1\Delta_2)\tilde{\gamma}_{j,\downarrow,+}\tilde{\gamma}_{j,\uparrow,-} \\
& - [\mu_1(t_2 + \Delta_2) + \mu_2(t_1 - \Delta_1)]\tilde{\gamma}_{j,\downarrow,+}\tilde{\gamma}_{j+1,\uparrow,-} - [\mu_1(t_2 - \Delta_2) + \mu_2(t_1 + \Delta_1)]\tilde{\gamma}_{j+1,\downarrow,+}\tilde{\gamma}_{j,\uparrow,-} \\
& - (t_1 - \Delta_1)(t_2 + \Delta_2)\tilde{\gamma}_{j,\downarrow,+}\tilde{\gamma}_{j+2,\uparrow,-} - (t_1 + \Delta_1)(t_2 - \Delta_2)\tilde{\gamma}_{j+2,\downarrow,+}\tilde{\gamma}_{j,\uparrow,-} \}, \\
& = H_{||,1} + H_{||,2}.
\end{aligned} \tag{20}$$

The transformation provided is a permutation of the block-diagonalizing transformation supplied by the unitary symmetry used in Eq. (17). This indicates that the separation of the Hamiltonian in real-space Majorana representation is also a consequence of the unitary symmetry, which in turn emerges from the chiral symmetries. Therefore, the resulting blocks in this representation are real-space, Majorana basis complements to the component Bloch Hamiltonians.

Subsequently, we may view the problem as two separate systems as shown in Figs. 4(a) and 4(b) and then consider a case-by-case approach. We again denote these two commuting parts, *component Hamiltonians*, by $H_{||,1}$ and $H_{||,2}$. We assume without loss of generality that $t_i = \Delta_i$, $i \in \{1, 2\}$, and we explore the different phases derived from Figs. 4(c) and 4(d) corresponding to the phases of the parent Hamiltonians.

Case 1. The first parent is topological with $\mu_1 = 0$ and the second one is trivial with $\mu_2 > 2t_2$. This is illustrated in Figs. 4(f) and 4(k) and Figs. 4(g) and 4(m) for components $H_{||,1}$ and $H_{||,2}$, respectively. One may notice that the graph in the bulk is isomorphic to the Kitaev chain. The condition $\mu_2 > 2t_2$ implies that the KC in (g) is topological with two Majorana zero modes in addition to the two Majoranas provided by the $\mu_1 = 0$ condition in (f). Consequently, we have four Majorana edge modes, all situated at the first and last sites of the MKC parallel system.

Case 2. The second parent is topological with $\mu_2 = 0$ and the first one is trivial with $\mu_1 > 2t_1$. This leads to a similar situation to that in Case 1 with respect to the position of the Majorana zero modes, and it is illustrated by Figs. 4(e) and 4(i) and Figs. 4(h) and 4(o) for components $H_{||,1}$ and $H_{||,2}$ respectively. We again have four Majorana zero modes, two from each component at the first and last sites of the MKC parallel system. However, we note that the pseudospin configuration at the first site and the last sites are parallel, unlike in Case 1, in which the pseudospins are antiparallel.

Case 3. Both parents are topological, i.e., $\mu_1 = 0$, $\mu_2 < 2t_2$ and $\mu_1 < 2t_1$, $\mu_2 = 0$. This case is illustrated by Figs. 4(k) and 4(m) and Figs. 14(n) and 14(p) for the components $H_{||,1}$ and $H_{||,2}$, respectively. Observe that no Majorana zero modes are present in $H_{||,2}$, while for $H_{||,1}$ we have Majorana zero modes at positions 1, 2 and $L - 1$, L for L sites.

Primarily, these results are exactly what we expect from our analysis of the bulk topology from Fig. 3. When both parents are topological, we have winding number $2 \oplus 0$. This corresponds to case 3, where we have two unpaired Majoranas at each edge of the component Hamiltonian $H_{||,1}$. This ultimately results in two pairs of unpaired Majoranas in the child. Furthermore, cases 1 and 2 have winding number $1 \oplus 1$, which corresponds to one Majorana at the edge of each component Hamiltonian, and four unpaired Majoranas in total.

Although in this case each of the Majoranas is on the same lattice site, they do not hybridize due to the protecting unitary symmetry. Ultimately, this illustrates that the tensor product structure leads to novel edge phenomena protected by bulk symmetries of the parents.

1. Edge states of the MKC parallel system from the component Hamiltonians and entanglement

We are finally in the position to discuss the full analytical expressions for the MZMs. We start with the Bloch component Hamiltonians $H_{||,1}$ and $H_{||,2}$ derived from the MKC parallel system, and we analyze their edge physics. We study decaying modes, therefore we take the limit in which our momenta is imaginary, $k \rightarrow iq$. Hence, after this limit, $H_{||,1}$ and $H_{||,2}$ are given as

$$\begin{aligned}
\mathcal{H}_{||,1}(iq) &= -[(\mu_1 + 2t_1 \cosh q)(\mu_2 + 2t_2 \cosh q) \\
&+ 4\Delta_1\Delta_2 \sinh^2 q]\sigma^z \\
&+ i[2\Delta_1 \sinh q(\mu_2 + 2t_2 \cosh q) \\
&+ 2\Delta_2 \sinh q(\mu_1 + 2t_1 \cosh q)]\sigma^y, \tag{21a}
\end{aligned}$$

$$\begin{aligned}
\mathcal{H}_{||,2}(iq) &= -[(\mu_1 + 2t_1 \cosh q)(\mu_2 + 2t_2 \cosh q) \\
&- 4\Delta_1\Delta_2 \sinh^2 q]\sigma^z \\
&+ i[2\Delta_1 \sinh q(\mu_2 + 2t_2 \cosh q) \\
&- 2\Delta_2 \sinh q(\mu_1 + 2t_1 \cosh q)]\sigma^y. \tag{21b}
\end{aligned}$$

Now, we apply this Hamiltonian to a decaying ansatz, and we calculate the zero-energy solutions. This provides a constraint for each component Hamiltonian on the decay rate of the wave function:

$$\begin{aligned}
& [(2t_1 \cosh q + \mu_1) \mp 2\Delta_1 \sinh q] \\
& \times [(2t_2 \cosh q + \mu_2) \mp 2\Delta_2 \sinh q] = 0 \tag{22}
\end{aligned}$$

for the component $H_{||,1}$ and

$$\begin{aligned}
& [(2t_1 \cosh q + \mu_1) \mp 2\Delta_1 \sinh q] \\
& \times [(2t_2 \cosh q + \mu_2) \pm 2\Delta_2 \sinh q] = 0 \tag{23}
\end{aligned}$$

for the component $H_{||,2}$. From the schematic diagrams Fig. 4, the two unpaired MZMs on each edge may be on the same site or neighboring sites. We study this in detail by considering the condition Eq. (22) for $\text{sgn}(t_i) = \text{sgn}(\Delta_i)$, $i \in \{1, 2\}$,

$$\begin{aligned}
& [(2t_1 \cosh q + \mu_1) - 2\Delta_1 \sinh q] \\
& \times [(2t_2 \cosh q + \mu_2) - 2\Delta_2 \sinh q] = 0. \tag{24}
\end{aligned}$$

If both the parents are topological, and $\frac{\mu_1}{\mu_2} = \frac{\Delta_1}{\Delta_2} = \frac{t_1}{t_2}$ —which is satisfied when both parents are identical—then $\mathcal{H}_{||,2}$ vanishes. We then solve for the spinors by substituting the

TABLE I. Null eigenvectors of the MKC parallel system for different topological characterizations of the two parent systems, ratio of signs of t_i and Δ_i , $i \in \{1, 2\}$, and boundary conditions.

Parent 1		Parent 2		MZM eigenvectors
Phase	$\frac{\text{sgn}(t_1)}{\text{sgn}(\Delta_1)}$	Phase	$\frac{\text{sgn}(t_2)}{\text{sgn}(\Delta_2)}$	
topo	+	topo	+	$\{\frac{1}{\sqrt{2}}(00\rangle - 11\rangle), 01\rangle, 10\rangle\}$ or $\{\frac{1}{\sqrt{2}}(00\rangle - 11\rangle), \frac{1}{\sqrt{2}}(01\rangle - 10\rangle)\}$
	+		-	$\{\frac{1}{\sqrt{2}}(01\rangle - 10\rangle), 00\rangle, 11\rangle\}$ or $\{\frac{1}{\sqrt{2}}(01\rangle - 10\rangle), \frac{1}{\sqrt{2}}(00\rangle + 11\rangle)\}$
	-		+	$\{\frac{1}{\sqrt{2}}(01\rangle + 10\rangle), 00\rangle, 11\rangle\}$ or $\{\frac{1}{\sqrt{2}}(01\rangle + 10\rangle), \frac{1}{\sqrt{2}}(00\rangle - 11\rangle)\}$
	-		-	$\{\frac{1}{\sqrt{2}}(00\rangle + 11\rangle), 01\rangle, 10\rangle\}$ or $\{\frac{1}{\sqrt{2}}(00\rangle + 11\rangle), \frac{1}{\sqrt{2}}(01\rangle + 10\rangle)\}$
topo	+	triv		$\{\frac{1}{\sqrt{2}}(00\rangle - 11\rangle), \frac{1}{\sqrt{2}}(01\rangle - 10\rangle)\}$
	-			$\{\frac{1}{\sqrt{2}}(00\rangle + 11\rangle), \frac{1}{\sqrt{2}}(01\rangle + 10\rangle)\}$
triv		topo	+	$\{\frac{1}{\sqrt{2}}(00\rangle - 11\rangle), \frac{1}{\sqrt{2}}(01\rangle + 10\rangle)\}$
			-	$\{\frac{1}{\sqrt{2}}(00\rangle + 11\rangle), \frac{1}{\sqrt{2}}(01\rangle - 10\rangle)\}$

conditions back into the Schrödinger equation. The full basis of the MKC parallel system is therefore given by four degrees of freedom, $(\tilde{c}_{k,\uparrow}, \tilde{c}_{k,\downarrow}, \tilde{c}_{-k,\uparrow}^\dagger, \tilde{c}_{-k,\downarrow}^\dagger)^T$, by combining the degrees of freedom of the two components. In this basis, the null eigenvectors derived from $\mathcal{H}_{||,1}(iq)$ are given as

$$|\Psi\rangle_{\text{MMZM}} = \left\{ \frac{1}{\sqrt{2}}(|00\rangle - |11\rangle), |01\rangle, |10\rangle \right\}, \quad (25)$$

where $|0\rangle = (1, 0)^T$, $|1\rangle = (0, 1)^T$. If the parameters are not commensurate, we instead have the eigenvectors

$$|\Psi\rangle_{\text{MMZM}} = \left\{ \frac{1}{\sqrt{2}}(|00\rangle - |11\rangle), \frac{1}{\sqrt{2}}(|01\rangle - |10\rangle) \right\}. \quad (26)$$

Next, say only parent 1 is topological and parent 2 is trivial, only the first factor in Eq. (24) can be set to zero. Substituting into Eqs. (21a) and (21b), the eigenvectors in the full basis with four degrees of freedom are shown to be

$$|\Psi\rangle_{\text{MMZM}} = \left\{ \frac{1}{\sqrt{2}}(|00\rangle - |11\rangle), \frac{1}{\sqrt{2}}(|01\rangle - |10\rangle) \right\}. \quad (27)$$

We would get the same eigenvectors if only parent 2 had been topological except that the functional form of the decaying ansatz would instead depend on parent 2 parameter values. Detailed calculations can be found in Supplemental Material Sec. S1 A [27]. Interestingly, by changing the topological character of one of the parents or the parameters becoming incommensurate, it is possible to transition from a product state to a maximally entangled Bell state. We list all the possible eigenvectors for different combinations of topology of the parents and signs of t_i compared to Δ_i in Table I.

Here it is important to remember that in each case, one has *four* eigenvectors. The table lists only the states at edge $x = 0$. The eigenvectors at the other edge can be found by changing $\frac{\text{sgn}(t_i)}{\text{sgn}(\Delta_i)}$ from + to - and *vice versa* for both parents. We will recover a total of four eigenvectors with two common eigenvectors for both signs when both parents are topological and the parameters are commensurate.

2. Spatial distribution of MZM wave functions for N -site MKC

We now characterize MZM wave functions in the MKC parallel lattice with N sites by computing the associated spatially resolved probability density for these states. This is critical in highlighting the fact that the zero modes are truly localized topological edge states. For the specific parameters, $\mu_1 = \mu_2 = 0$ for $t_1 = \Delta_1$ and $t_2 = \Delta_2$, we exist in the dimerized limit and therefore the wave function must be a δ function at the two edges. As seen from the schematic diagram Fig. 4, two more δ functions are situated at site indices $j = 2$ and $j = N - 1$. We illustrate this with a numerical simulation for this specific case in Fig. 5.

Tuning away from this limit, we expect the δ functions to broaden while still remaining localized at the edges. We compare and contrast the Kitaev chain and the MKC in terms of probability density distributions for topologically protected in-gap states. These results are shown in Fig. 6. Similarly to the Kitaev chain, we observe that the MKC zero modes can be spatially separated from each other, with their probability densities peaking near opposite ends of the chain and on sites

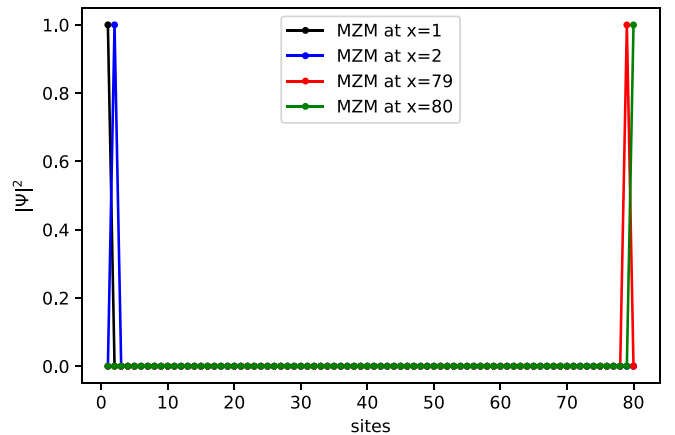


FIG. 5. MZMs for the MKC parallel system with $N = 80$ sites for the parameter values $\mu_1 = \mu_2 = 0$, $t_1 = \Delta_1 = 1$, and $t_2 = \Delta_2 = 1$ obtained numerically. We observe MZMs at site indices 1, 2, 79, and 80 as inferred previously from the schematic diagram.

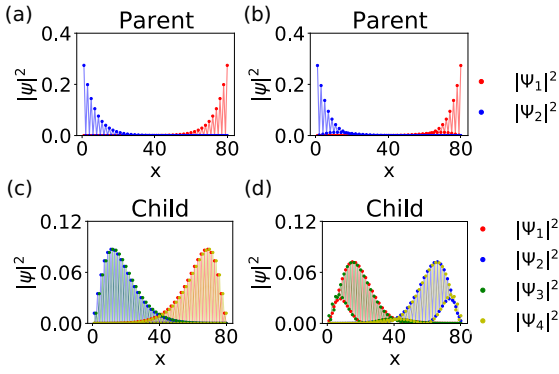


FIG. 6. (a) Bound states for the Kitaev chain in the topological region with $t = 1$, $\Delta = 0.08$, and $\mu = 0$. (b) Ground states for the Kitaev chain for $t = 1$, $\Delta = 0.08$, and $\mu = 0.09$. (c) Bound states for a multiplicative chain with two identical parents in the topological phase, each shown in subfigure (a). Here $\Psi_{1,2} = \Psi'_1 \pm \Psi'_3$ and $\Psi_{3,4} = \Psi'_2 \pm \Psi'_4$, with Ψ' an eigenvector of the finite Hamiltonian. (d) Bound states for a multiplicative chain with two identical parents in the topological phase, each shown in subfigure (b). Here $\Psi_{1,2} = \Psi'_1 \pm \Psi'_4$ and $\Psi_{3,4} = \Psi'_2 \pm \Psi'_3$, with Ψ' an eigenvector of the finite Hamiltonian.

of different parity. When there are four degenerate zero modes in the MKC, two are localized at each end of the chain, instead of one zero mode localized at each end of the Kitaev chain.

Furthermore, the boundary modes of the child Hamiltonian peak in probability density away from the ends of the chain, though they are still predominantly near one end or the other. The nature of the decay depends on the size of the bulk gap, which is naturally smaller for the multiplicative model than the parents for small gaps.

3. Robustness of the MKC parallel MZMs

Before proceeding further, one must check for the robustness of the MZMs for the MKC parallel system to local disorder. We know that for the two-band Kitaev chain, the MZMs persist when subject to local disorder proportional to σ^z and σ^y in the particle-hole basis. Only when the local disorder is proportional to σ^x in the particle-hole basis are the MZMs shifted from zero energy (see Fig. 7). We similarly investigate the effects of myriad disorder terms for the MKC parallel system. We have both the particle-hole and

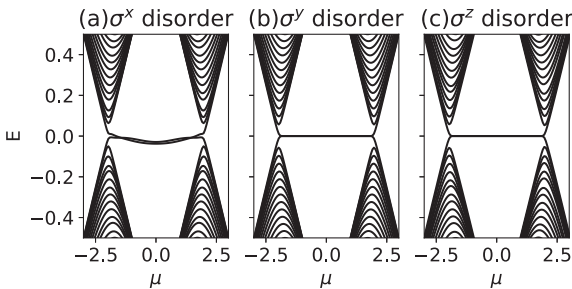


FIG. 7. Checking the robustness of Kitaev chain to disorder proportional to (a) σ^x , (b) σ^y , and (c) σ^z . MZMs are robust for σ^y and σ^z disorder while they break off from zero energy for σ^x disorder.

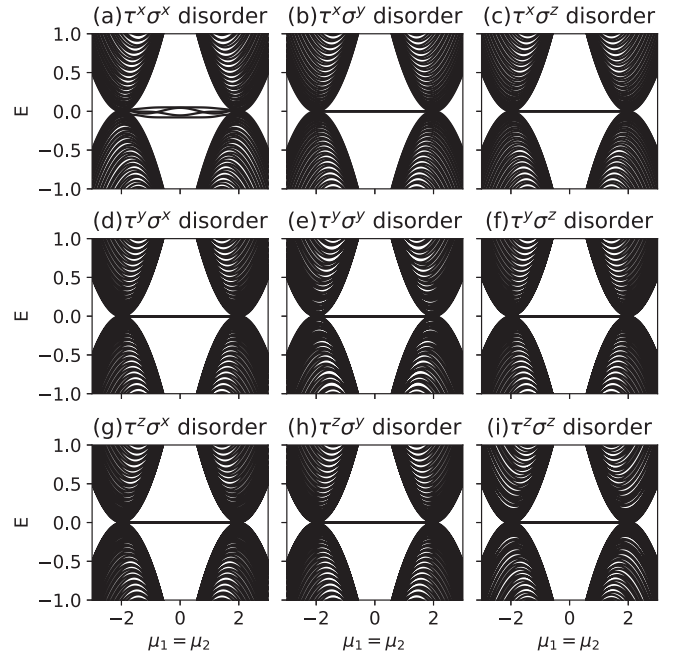


FIG. 8. Checking for robustness of the MKC parallel MZMs in the presence of various on-site disorders with magnitude $0.2t$. In the case $\mu_1 = \mu_2$, only the on-site disorder proportional to $\tau^x\sigma^x$ perturbs the MZMs from zero energy, signifying that the MZMs in the parallel MKC system are naturally more robust than their constituent parents.

pseudospin basis in this case, however, so we must check for all possible tensor-product combinations of local disorder. We observe that the MZMs persist at zero energy for local disorder proportional to any of the combinations $\tau^i\sigma^j$, where $i, j \in \{0, y, z\}$ if at least one of the parents is topological. Also it is robust to local disorder proportional to $\tau^z\sigma^x$, $\tau^x\sigma^z$, $\tau^y\sigma^x$, and $\tau^x\sigma^x$ if both parents are topological (see Fig. 8). The flat midgap states corresponding to the MZMs only break down when the local disorder is proportional to $\tau^x\sigma^x$ even if one of the parents is topological. This suggests that the MKC parallel child MZMs are more robust than those of its parents.

4. Quantum gate operations without braiding

According to Table I, numerous separable and maximally entangled two-qubit states are realized by the MKC. For instance, if each parent KC is in the topological phase and the sign of $\frac{t_i}{\Delta_i}$ is $+$ for each i , with $i \in \{1, 2\}$, one realizes the Bell state $\frac{1}{\sqrt{2}}(|00\rangle - |11\rangle)$ and the separable states $\{|01\rangle, |10\rangle\}$. This situation can be easily reversed by changing the sign of $\frac{t_2}{\Delta_2}$ to $-$, so that the Bell state instead takes the form $\frac{1}{\sqrt{2}}(|01\rangle - |10\rangle)$, while the separable states are instead $\{|00\rangle, |11\rangle\}$. Other combinations of separable state sets or maximally entangled states are possible, although only one parity possesses entanglement at a given point in phase space when both parent systems are topological. Moreover, if one wants to retain the entanglement of the complement parity while converting the separable set of states to a Bell state, one tunes one of the parents through phase space until it undergoes a topological phase transition to its trivial phase. As transport of the MKC through phase space corresponds to preparation of particular

two-qubit states, including qubit entanglement, multiplicative topological phases have some potential as platforms for topologically protected quantum computation schemes. First, there is the interesting possibility of using the degenerate manifold of states for the case of each parent topological, in braiding-based topological quantum computation schemes, despite the resultant MKC corresponding to an even number of particles in the ground state. Second, there also appears to be the potential for topological quantum computation schemes based on tuning the system through topological phase transitions of the parents in combination with changes in parity of certain parameter ratios. This possibility of “phase space” topological quantum computation schemes will be explored in future work.

C. Finite MKC parallel system with open boundary conditions

Having presented the bulk spectrum of the multiplicative Kitaev chain, as well as the corresponding edge phenomena, we study the parallel MKC in the small finite lattice regime. This regime is physically relevant for realistic systems, and it has been shown to yield novel topological effects [28]. To do so, we characterize the MZMs realized in topologically nontrivial regions of the phase diagram analytically for the case of parallel parent Kitaev chains. We then numerically study the low-energy spectrum as a function of chain length L and chemical potentials μ_1 and μ_2 , as well as analytically deriving the edge states in the small lattice size limit.

1. Spectral dependence on chain length

While the finite Kitaev chain can realize unpaired Majorana *zero modes*, this is contingent on the bound states not overlapping and thus hybridizing. In general, there is actually a finite split in energy between the topologically protected bound states due to wave-function overlap. The dependence of the finite Kitaev chain spectrum for open boundary conditions is therefore typically studied to demonstrate that this splitting decreases exponentially with increasing system size. We thus study the spectral dependence of the MKC with open boundary conditions as a function of chain length for direct comparison.

For the topologically protected pair of low-energy modes localized on the boundary of the finite-length Kitaev chain described by H_{BdG} given in Eq. (3) for OBC to be at $E = 0$, the parameters t , μ , and Δ need to be fine-tuned [29]. Otherwise, as shown in Fig. 9(a), these boundary mode energies oscillate as a function of chain length L with a period determined by μ/Δ [29] while also decreasing overall in exponential fashion.

Comparatively, the finite multiplicative chain also presents an oscillatory dependence on ground-state energy with respect to chain length when at least one of the parents is in the topological phase. Figure 9 shows the spectral dependence of the finite multiplicative Kitaev chain $H_{\text{MKC},\parallel}^c(k)$ in Eq. (8) for two key cases:

(i) The parameter sets of parents 1 and 2 are equal, meaning $t_1 = t_2$, $\Delta_1 = \Delta_2$, and $\mu_1 = \mu_2$, and each parent is topologically nontrivial. The low-energy spectrum of the parents for this case is shown in Fig. 9(a), and the corresponding

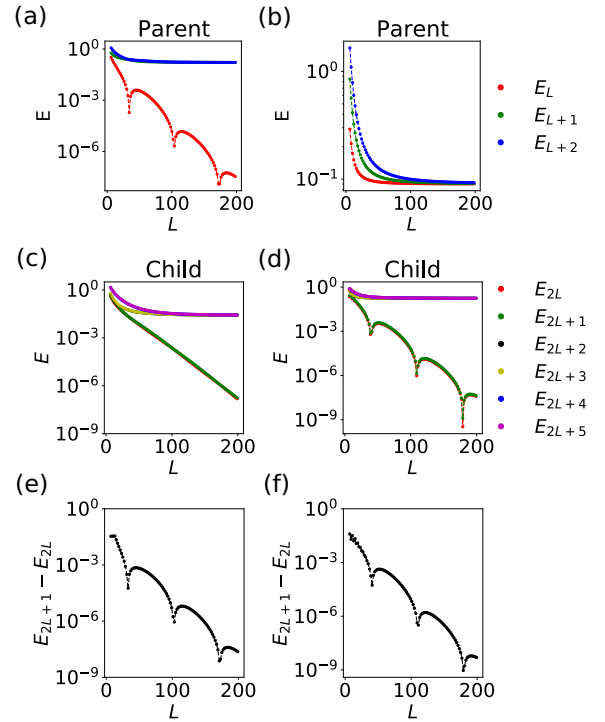


FIG. 9. Low-energy spectrum vs chain length L for the Kitaev chain shown in (a) and (b) and for the parallel MKC Hamiltonian $H_{\text{MKC},\parallel}^c(k)$ shown in (c)–(f). Each plot shows the spectrum only for even values of L . (a) The three lowest-energy modes of the Kitaev chain Hamiltonian in the topological phase with open boundary conditions, corresponding to $t = 1$, $\Delta = 0.08$, $\mu = 0.09$, as a function of chain length L . (b) The three lowest-energy modes of the Kitaev chain Hamiltonian in the trivial phase corresponding to $t = 1$, $\Delta = 0.08$, $\mu = 2.09$. (c) The six lowest-energy modes of the MKC Hamiltonian with two parent Kitaev chains that each have a parameter set corresponding to (a). (d) The six lowest-energy modes of the MKC Hamiltonian with a parent Kitaev chain with parameter set corresponding to subfigure (a) and the second parent Kitaev chain with parameter set corresponding to subfigure (b). (e),(f) Energy difference between the two lowest energies in (c),(d), indicating their nondegeneracy.

low-energy spectrum of the child Hamiltonian is shown in Figs. 9(c) and 9(e).

(ii) Parent 1 is topologically nontrivial and Parent 2 is topologically trivial. The low-energy spectra of parents 1 and 2 for this case are shown in Figs. 9(a) and 9(b), respectively. The corresponding low-energy spectrum of the child Hamiltonian is shown in Figs. 9(d) and 9(f).

In each case, the child Hamiltonian exhibits oscillations in the two lowest-energy modes $E_{2L+1} - E_{2L}$, indicating splitting of the ground-state degeneracy due to finite-size effects. A key difference is that the child exhibits negligible Friedel oscillations relative to zero energy in case 1 as shown in Fig. 9(c), although there is evidence of Friedel oscillations in the splitting in energy between these two lowest energy states as shown in Fig. 9(e). Friedel oscillations are significantly more dramatic in the low-energy child spectrum for case 2 as shown in Fig. 9(d), although splitting in energy between the two lowest energy states is very similar to case 1 as shown in

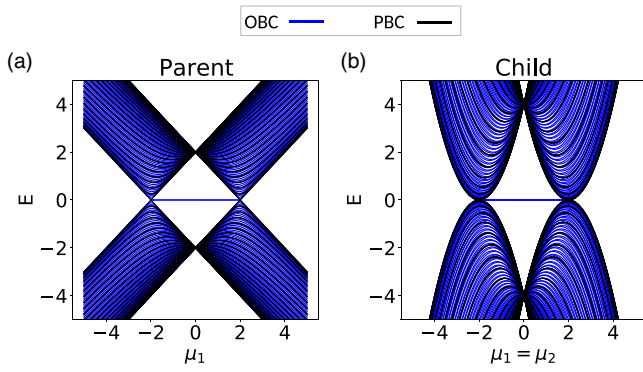


FIG. 10. Spectra of the parent and child Hamiltonians as a function of chemical potential for relatively long chain length $L = 80$, shown in black for periodic boundary conditions and blue for open boundary conditions, respectively. The spectra for parents 1 and 2 are identical as their parameter sets are identical, thus the spectrum for parent 1 is shown in (a) for $t_1 = t_2 = 1$, $\Delta_1 = \Delta_2 = 1$, $\mu_1 = \mu_2$. The corresponding child MKC spectrum is shown in (b) as a function of μ_1 , with $\mu_2 = \mu_1$.

Fig. 9(f). Fundamentally, we still observe a localization of the zero modes with respect to system size.

2. Spectral dependence on chemical potential of finite MKC

The competition between the chemical potential μ and kinetic energy t controls the phase diagram of parent Kitaev chains, and therefore it is also important in understanding behavior of the MKC. Much can be learned, in particular, by studying the spectra of the parent Kitaev chains and MKC as a function of chemical potential, specifically the regions in which MZMs may form. The dependence of the eigenenergies with respect to μ are shown for the parent and child in Figs. 10(a) and 10(b), respectively, for a long chain length of $L = 80$. Importantly, we observe a topological phase transition in the parent for $\mu_1 = \pm|2t_1|$ due to closing of the bulk gap as expected, with states dispersing linearly when tuning μ_1 away from these critical values. For $-2t_1 < \mu_1 < 2t_1$, we see low-energy modes inside the bulk gap, corresponding to the unpaired Majorana zero modes localized at each end of the chain. Comparing this to the spectrum for the MKC, we see clear similarities for μ_2 fixed in value to μ_1 : the bulk gap also closes at $\mu_1 = \pm|2t_1|$ as the system undergoes topological phase transitions, with $-2t_1 < \mu_1 < 2t_1$ again corresponding to a topologically nontrivial phase and the presence of topologically protected boundary modes. The spectrum instead disperses quadratically as μ_1 and μ_2 are tuned away from the critical values, and the maximum bulk gap is larger, being the product of the maximum bulk gaps of the parents. This multiplicative structure also yields a fourfold degeneracy of the in-gap states, compared with a twofold degeneracy of the in-gap states for the parents. More generally, the degeneracy of states for the child is twice that of each parent.

We also explore the dependence of the multiplicative spectrum on chemical potential for relatively short chain length. Here, edge modes overlap and therefore hybridize, however one sees that zero modes still remain at a finite number of μ values [28]. These results are shown in Fig. 11. While the spectra for periodic boundary conditions display bulk gap

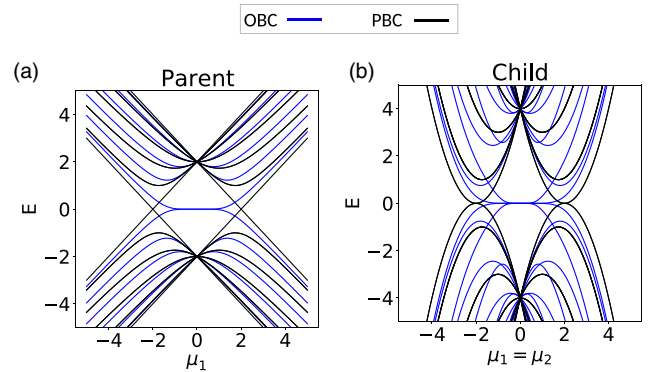


FIG. 11. Spectra of the parent and child Hamiltonians as a function of chemical potential for relatively short chain length $L = 6$, with black lines depicting spectra for periodic boundary conditions and blue lines depicting spectra for open boundary conditions, respectively. The spectra for parents 1 and 2 are identical as their parameter sets are identical, thus the spectrum for parent 1 is shown in (a) for $t_1 = t_2 = 1$, $\Delta_1 = \Delta_2 = 1$, $\mu_1 = \mu_2$. The corresponding child MKC spectrum is shown in (b) as a function of μ_1 , with $\mu_2 = \mu_1$.

closings at the same values of μ_1 and states disperse linearly as μ_1 is tuned away from these critical values between the $L = 80$ case and the $L = 6$ case, striking differences are observed for open boundary conditions. In particular, gap-closings occur at $\mu_1 = 0$ rather than $\mu_1 = \pm|2t_1|$ in the parents, as shown in Fig. 11(a), due only to destructive interference between states resulting from bulk-boundary correspondence. In addition, the fourfold degeneracy of the in-gap states for the child, shown in Fig. 11(b), is split away from $\mu_1 = 0$, with the energy gap between two states increasing more rapidly with increasing $|\mu_1|$ than for the other two states.

While the finite Kitaev chain is known to have exact zero-energy modes for discrete values of the chemical potential [29] given by $\mu_n = 2\sqrt{t^2 - \Delta^2} \cos(\frac{n\pi}{L+1})$ with $n \in \{1, \dots, L\}$, which we refer to as *Majorana points*, these Majorana points are clear in the short chain regime as they are sparse and split the topological region into large separate domains. As the chain length increases, these Majorana points proliferate through the μ range within the topological region and form a flat plateau of zero modes. The multiplicative short finite chain does not present exact zero-energy modes for identical parent Hamiltonians with equal parameter sets such that $t_1 = t_2$, $\Delta_1 = \Delta_2$, and $\mu_1 = \mu_2$, unless $\frac{t_1}{\Delta_1} = \frac{t_2}{\Delta_2} = 1$. The latter configuration is represented in Fig. 11, where the exact zero-energy dependence on the chemical potential of a multiplicative chain is qualitatively similar to the behavior of its two identical parents. Finite-size effects can lead to more significant differences between parent and child spectra, however. As shown in Fig. 12 for $|\frac{t_1}{\Delta_1}| = |\frac{t_2}{\Delta_2}| = 2$, the presence of exact zero modes in both identical parents, shown in Figs. 12(a) and 12(b) for different chain lengths, does not imply that a finite multiplicative chain also possesses exact zero modes. In fact, we observe in Figs. 12(c)–12(f) that if $t_i \neq \Delta_i$, the parents must be nonidentical for the child to have exact zero modes, considering the example for which $\text{sgn}(\frac{t_1}{\mu_1}) = -\text{sgn}(\frac{t_2}{\mu_2})$. Identical parents are shown by Figs. 12(c) and

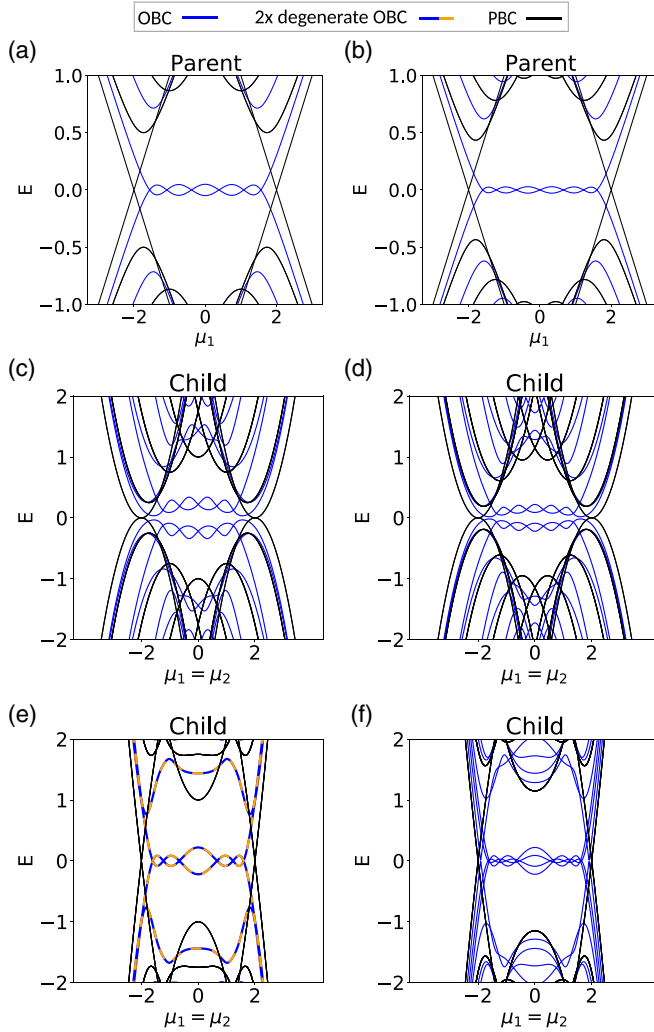


FIG. 12. Child and parent spectrum dependence on the chemical potential. Kitaev chain spectrum for parameters $|t| = 1$, $\Delta = 0.5$ for even and odd chains ($L = 6, 7$) is shown in (a) and (b), respectively. Multiplicative chain spectrum for two identical parents as in (a) and (b) is shown in (c) and (d), respectively. Multiplicative chain spectrum for two different parents with $t_1 = -t_2 = 1$, $\Delta_1 = \Delta_2 = 0.5$ and even and odd chains ($L = 6, 7$) is shown in (e) and (f), respectively. The black curves correspond to solutions under periodic boundary conditions, which are all doubly degenerate for the children. The blue curves correspond to open boundary conditions, with double-degeneracy indicated by dashed blue-orange curves.

12(d) for different chain lengths. In these cases, exact zero energies are not obtained in finite chains.

The spectral dependence on the chemical potential reveals interesting differences between the multiplicative chain and its parents. In the latter, the number of zero modes is given by the chain's length L [see Figs. 12(a) and 12(b)], while in the former the parity of the number of zero modes is always even when the necessary conditions $\frac{t_1}{\Delta_1} \neq 1$ and $\frac{t_2}{\Delta_2} \neq 1$ for exact zero modes with distinct parents are satisfied, regardless of the chain length's parity [see Figs. 12(e) and 12(f)]. Furthermore, dependence of the child spectra on free parameters shows greater variety than expected: the spectra shown in Figs. 12(c) and 12(d), for instance, display a quadratically dispersing

child spectrum, which results quite naturally from the child's tensor product combination of two linearly dispersing Kitaev Hamiltonians. This is a fairly general characteristic of multiplicative models. However, a linear dispersion can be obtained when $\text{sgn}(\frac{t_1}{\mu_1}) = -\text{sgn}(\frac{t_2}{\mu_2})$, as shown in Figs. 12(e) and 12(f). Both the quadratic and linear dispersions are explained in Supplemental Material, Sec. S4 [27] in Eqs. S82 and S84. Such results demonstrate the rich interplay between finite-size topology and multiplicative topological phases.

3. Analytical theory of finite size parallel MKC edge states

Using the diagrammatic approach from previous sections, we can gain greater understanding of the exact zero modes prominent for finite-size MKC. In Figs. 12(e) and 12(f), we observe that for the parameters $|t_i| = 2|\Delta_i|$, $i \in \{1, 2\}$, and $t_1 = -t_2$, one gets bubbles for the two energy levels near zero versus $\mu_1 = \mu_2$. Notably, there is a difference in the positions of the zero energy or Majorana points between systems with an even versus odd number of lattice sites in a finite-size MKC parallel system. Systems with an even number of sites, as shown in Fig. 12(e), exhibit a twofold degeneracy in the spectrum, here highlighted by dashed blue and orange lines, while systems with an odd number of sites exhibit more complex structure for the low-energy states occurring for open-boundary conditions as shown in Fig. 12(f). The rich structure in this case is a consequence of the full chain consisting of two decoupled subsystem chains. This is derived in the schematic diagram Fig. 13 from Fig. 4(b) corresponding to $H_{||,2}$. As shown in Figs. 12(a) and 12(b), the number of Majorana points in the parent systems varies with chain length. As a result, the spectra of the two subsystem chains will not coincide when the subsystems are of different chain length.

We can see when $\mu_1 = \mu_2 = \mu$, $t_1 = -t_2 = -t$, $\Delta_1 = \Delta_2 = \Delta$, the component Hamiltonian, $H_{||,2}$ in Eq. (18b), possesses only next-nearest-neighbor interactions. Thus, we can split the chain into two KCs such that the number of sites is conserved. Then for a system with $2L$ lattice sites, we get two KCs of length L , while for a system with $2L + 1$ sites, we get two KCs of length L and $L + 1$, respectively. We know that for an L -site KC with parameters μ' , t' , and Δ' , the zero-energy Majorana points are found at $\mu' = 2\sqrt{t'^2 - \Delta'^2} \cos \frac{n\pi}{L+1}$, where $n \in \{1, \dots, L\}$ i.e., there are L Majorana points. We apply a similar calculation to our KCs with the mapping $\mu' = \mu^2 - 2t^2 + 2\Delta^2$, $t' + \Delta' = -(t + \Delta)^2$, $t' - \Delta' = -(t - \Delta)^2$ derived from Fig. 13. Then we get the following identity:

$$\begin{aligned} \mu &= \pm \sqrt{2(t^2 - \Delta^2) \left(1 + \cos \frac{n\pi}{L+1}\right)}, \quad n \in \{1, \dots, L\}, \\ \Rightarrow \mu &= 2\sqrt{t^2 - \Delta^2} \cos \frac{n\pi}{2L+2}, \quad n \in \{1, \dots, 2L+2\}, \end{aligned} \quad (28)$$

for exact zero modes in each of the split KC systems of length L .

From this calculation, we infer that $H_{||,2}$ with $2L$ sites corresponds to $2L$ Majorana points, which are twofold degenerate in this limit. Similarly, $H_{||,2}$ with $2L + 1$ sites produces $2L \oplus 2(L + 1)$ Majorana points due to contributions from each of

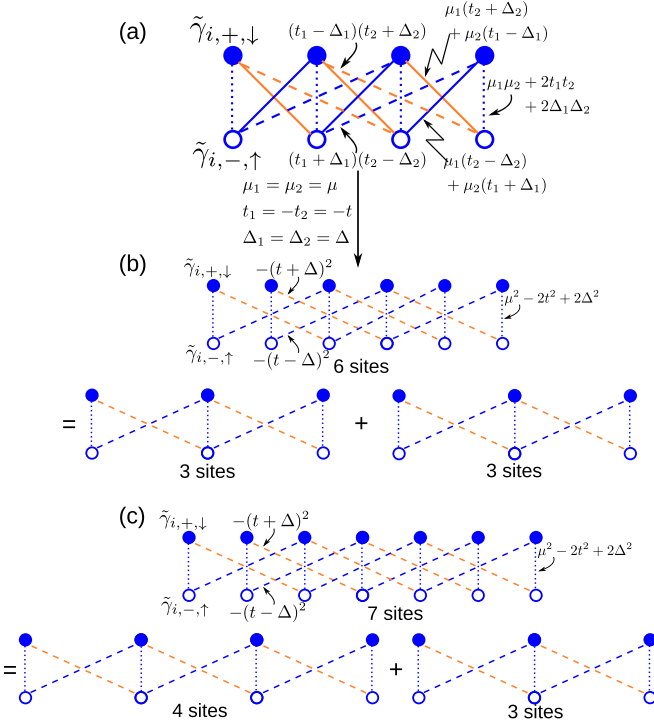


FIG. 13. Schematic diagram of $H_{||,2}$ (a) for the particular case $\mu_1 = \mu_2 = \mu$, $t_1 = -t_2 = -t$, $\Delta_1 = \Delta_2 = \Delta$, and $t \neq \Delta$. Illustrating for the cases (b) $L = 6$ and (c) $L = 7$, the system can now be broken down to two three-site KCs or one four-site and another three-site KC. The zero-energy Majorana points can be explained from here.

the two subsystem KCs. The set of μ values corresponding to Majorana points derived from Eq. (28), $\{\mu_i\}$, agrees with the Majorana points shown from the numerical simulation in Figs. 12(e) and 12(f).

We supplement our understanding of the diagrammatic approach by analyzing boundary conditions on the edge state wave functions when $t_1 \neq \Delta_1$ and/or $t_2 \neq \Delta_2$, in finite-size lattices. Considering Eq. (24), we obtain four values for e^{-q} ,

$$e^{-q} = \frac{-\mu_1 \pm \sqrt{\mu_1^2 - 4(t_1^2 - \Delta_1^2)}}{2(t_1 + \Delta_1)} \quad \text{and} \quad \frac{-\mu_2 \pm \sqrt{\mu_2^2 - 4(t_2^2 - \Delta_2^2)}}{2(t_2 + \Delta_2)}. \quad (29)$$

We require standing-wave solutions for the finite-size lattice, which require that our four e^{-q} values transform to $R_1 e^{\pm i\theta_1}$ and $R_2 e^{\pm i\theta_2}$, respectively. Hence, we propose a general form for the wave function,

$$\Psi(l) = A_1 R_1^l e^{il\theta_1} + A_2 R_1^l e^{-il\theta_1} + B_1 R_2^l e^{il\theta_2} + B_2 R_2^l e^{-il\theta_2}, \quad (30)$$

where A_1 , A_2 , B_1 , and B_2 are constants, and l is the site index. From recurrence relations derived from Eq. (24) (via the alternative equivalent chiral decomposition) [30], one has open boundary conditions at the artificial sites outside the lattice, i.e., $\Psi(l=0) = \Psi(l=-1) = 0 = \Psi(l=N+1) = \Psi(l=N+2)$. From these four boundary conditions, it is

possible to derive a quantization condition for the existence of any MZM standing-wave eigenfunction on a finite lattice of size N , which we have derived in Supplemental Material [27], Sec. S1 A,

$$\frac{R_1^{2(N+2)} + R_2^{2(N+2)} - 2R_1^{N+2}R_2^{N+2} \cos(2(N+2)\theta_+)}{R_1^2 + R_2^2 - 2R_1R_2 \cos 2\theta_+} = \frac{R_1^{2(N+2)} + R_2^{2(N+2)} - 2R_1^{N+2}R_2^{N+2} \cos(2(N+2)\theta_-)}{R_1^2 + R_2^2 - 2R_1R_2 \cos 2\theta_-}, \quad (31)$$

where $\theta_{\pm} = \frac{1}{2}(\theta_1 \pm \theta_2)$.

Now we construct the wave function for the case in which we have Majorana points, namely Figs. 12(e) and 12(f), where $t_1 = -t_2$ and $\Delta_1 = \Delta_2$. For this specific case, $R_2 e^{i\theta_2} = R_1 e^{i\pi} e^{i\theta_1}$ derived from the conditions for component Hamiltonian 2. Substituting this into our derived quantization condition, we can obtain values of μ with $\mu = 2\sqrt{t^2 - \Delta^2} \cos \frac{n\pi}{N+2}$, $n \in \{1, \dots, N+1\}$ for $N = \text{even}$ and $\mu = 2\sqrt{t^2 - \Delta^2} \cos \frac{n\pi}{N+1}$, $n \in \{1, \dots, N\}$ and $\mu = 2\sqrt{t^2 - \Delta^2} \cos \frac{n\pi}{N+3}$, $n \in \{1, \dots, N+2\}$ for $N = \text{odd}$. We note that these comprise the same list of μ values as gathered from our diagrammatic approach. From Eq. (30), one can show that we get two eigenfunctions for the MZMs at the Majorana points of the form

$$\Psi_1(l) \sim R_1^l [1 + (-1)^l] e^{il\theta_1} - R_1^l [1 + (-1)^l] e^{-il\theta_1}, \quad (32a)$$

$$\Psi_2(l) \sim R_1^{l+1} [1 + (-1)^{l+1}] e^{i(l+1)\theta_1^2} - R_1^{l+1} [1 + (-1)^{l+1}] e^{-i(l+1)\theta_1^2}, \quad (32b)$$

where for $N = \text{even}$ we have $\theta_1^1 = \theta_1^2 = \frac{n\pi}{N+2}$ and for $N = \text{odd}$ we have $\theta_1^1 = \frac{n\pi}{N+1}$ and $\theta_1^2 = \frac{n\pi}{N+3}$. The above expressions include only eigenfunctions localized at or near the left edge of the system. The eigenfunctions for the multiplicative Majoranas localized at or near the right edge can be derived analogously by the transformation $l \rightarrow N+1-l$. We have provided a comparison between our analytic derivation for the edge state wave function and its numerical counterpart in Fig. 14.

We can further use this quantization condition to process situations that fall outside this small range. For example, one may derive conditions for μ at different values of $\theta_2 - \theta_1 = \delta$ for $R_1 = R_2$, which is found for $|t_1/\Delta_1| = |t_2/\Delta_2|$. We illustrate the case for $\delta = \frac{2\pi}{3}$ in the Supplemental Material, Sec. S1 A [27].

IV. CHILD HAMILTONIAN FOR PERPENDICULAR PARENT CHAINS

To further explore the potential for multiplicative phases to realize exotic phenomena, we now characterize an MKC Hamiltonian with the two parent Kitaev chains which are *perpendicular* to one another, constructing a two-dimensional rather than one-dimensional MKC. That is, we take one parent Kitaev chain to lie along the \hat{x} -axis, and the second parent Kitaev chain to lie along the \hat{y} -axis, respectively. The parent

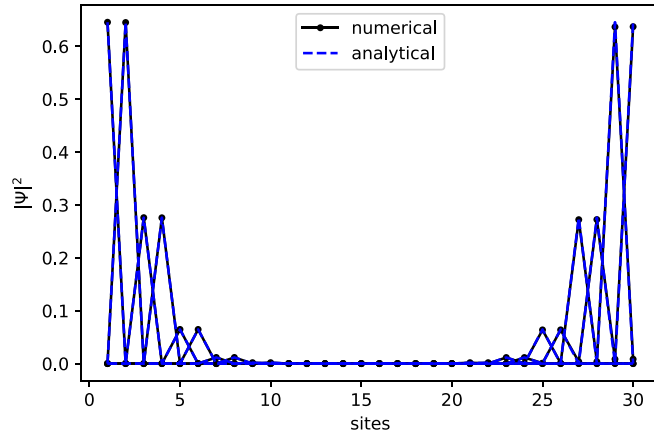


FIG. 14. We compare the numerically and analytically derived wave-function probability density for the MZMs in the parametric range $t_1 = -t_2 = -1$, $\Delta_1 = \Delta_2 = 0.5$, and $\mu_1 = \mu_2 = 2\sqrt{t_1^2 - \Delta_1^2} \cos(\pi/(N+2))$ for a lattice size, $N = 30$. We see that the numerical and analytical expressions match.

Hamiltonians and child Hamiltonian then take the following forms:

$$H_{p,1}(k_x) = -(2t_1 \cos k_x + \mu_1)\tau^z + 2\Delta_1 \sin k_x \tau^y, \quad (33a)$$

$$H_{p,2}(k_y) = -(2t_2 \cos k_y + \mu_2)\sigma^z + 2\Delta_2 \sin k_y \sigma^y, \quad (33b)$$

$$H_{\perp}^c(k_x, k_y) = [-(2t_1 \cos k_x + \mu_1)\tau^z + 2\Delta_1 \sin k_x \tau^y] \otimes [(2t_2 \cos k_y + \mu_2)\sigma^z + 2\Delta_2 \sin k_y \sigma^y]. \quad (33c)$$

This system is significantly different from the parallel MKC not only because the perpendicular orientation of the two parent chains yields next-nearest-neighbor (NNN) hopping along the $(\hat{x} \pm \hat{y})$ and $-(\hat{x} \pm \hat{y})$ directions, but also due to the absence of correlation between the two parent Hamiltonians in the expression for the edge modes, as we shall show.

We characterize the MKC in this case first by studying the bulk spectrum and then by studying bulk boundary correspondence analytically and numerically.

A. Bulk properties of the perpendicular MKC

In this subsection, we investigate the bulk properties of the perpendicular multiplicative Kitaev chain. First, we start with the properties of the bulk spectrum and then study the model's topological attributes.

1. Bulk spectrum for the perpendicular MKC

Similarly to the case of the parallel MKC, we first characterize the spectral properties of the perpendicular MKC bulk. We consider the simplest case here of two parent Hamiltonians with identical parameter sets but differing in that one is a function of momentum in the \hat{x} -direction, k_x , and the other is a function of momentum in the \hat{y} -direction, k_y . Each parent KC is in the topologically nontrivial phase, with a minimum direct gap of $2(2t_i - \mu_i)$ ($i = 1, 2$) at the edge of the Brillouin zone, which is 1 in this case, as shown in Figs. 15(a) and 15(b). Bands disperse quadratically near high-symmetry points 0 and π , respectively. The minimum direct band gap of the perpendicular MKC is analogously at $(k_x, k_y) = (\pi, \pi)$

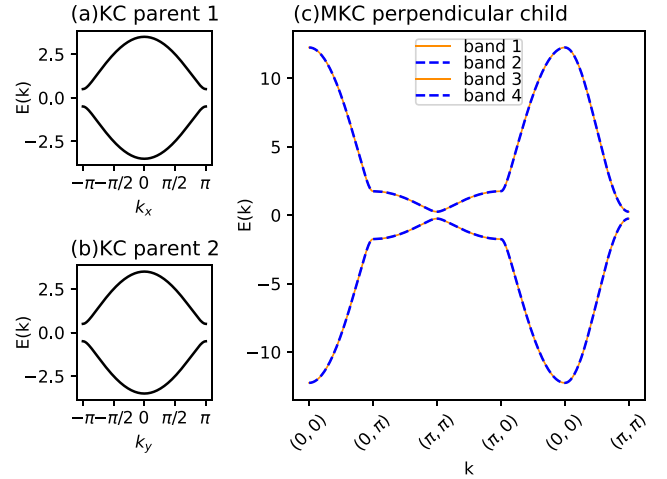


FIG. 15. The dispersion for (a) parent KC 1 ($t_1 = 1.0$, $\mu_1 = 1.5$, $\Delta_1 = 1.0$) along the k_x axis, (b) parent KC 2 ($t_2 = 1.0$, $\mu_2 = 1.5$, $\Delta_2 = 1.0$) along the k_y axis, and (c) the MKC perpendicular child from the two parents.

and $2(2t_1 - \mu_1)(2t_2 - \mu_2)$, which in this case is 0.5. This already shows greater variety in spectra of the perpendicular MKC when compared with the parallel case, where the eigenvalues of the MKC in the bulk are products of eigenvalues of the parent Kitaev chains in the bulk. The direct gap widens at $(k_x, k_y) = (\pi, 0)$ and $(0, \pi)$, approximately matching the value of each of the parent direct gaps, at $k_x = \pi$ or $k_y = \pi$, respectively. However, the direct gap widens significantly beyond the maximum direct gap of the parents at $(k_x, k_y) = (0, 0)$. This value reflects the multiplicative nature of the spectrum, being the square of the maximum direct gap of each parent.

2. Quasiparticle velocity near critical points

In the vicinity of a critical point, such as $\mu \sim -2t$, the two-band KC Dirac Hamiltonian exhibits quasiparticles that propagate with a constant velocity along the system's length when $k \sim 0$. Conversely, considering the MKC system with perpendicular axes, the corresponding Dirac Hamiltonian, for instance, when $\mu_1 \sim -2t_1$ and $k_x \sim 0$, is

$$H_{D,x}(k_x, k_y) = -m_1(2t_2 \cos k_y + \mu_2)\Gamma^{zz} + 2\Delta_1(2t_2 \cos k_y + \mu_2)k_x\Gamma^{yz} - 2m_1\Delta_2 \sin k_y\Gamma^{zy} + 4\Delta_1\Delta_2 k_x \sin k_y\Gamma^{yy}, \quad (34)$$

where $m_1 = 2t_1 + \mu_1$ and $\Gamma^{ij} = \tau^i\sigma^j$. The quasiparticles at this critical point correspond to the parent 1 system. The doubly degenerate energy is given as

$$E(k_x, k_y) = \pm\sqrt{4\Delta_1^2 k_x^2 + m_1^2} \times \sqrt{4\Delta_2^2 \sin^2 k_y + (2t_2 \cos k_y + \mu_2)^2}. \quad (35)$$

Expanding further around the critical point originating from the parent 2 system, near $\mu_2 \sim -2t_2$ when $k_y \sim 0$, reveals the

resulting Dirac Hamiltonian to be

$$\begin{aligned}
 H_{D,y}(k_x, k_y) = & -m_2(2t_1 \cos k_x + \mu_1)\Gamma^{zz} + 2m_2\Delta_1 \sin k_x \Gamma^{yz} \\
 & - 2\Delta_2(2t_1 \cos k_x + \mu_1)k_y \Gamma^{zy} \\
 & + 4\Delta_1\Delta_1 k_y \sin k_x \Gamma^{yy}, \quad (36)
 \end{aligned}$$

where $m_2 = 2t_2 + \mu_2$. The doubly degenerate energy in this case is

$$\begin{aligned}
 E(k_x, k_y) = & \pm \sqrt{4\Delta_1^2 \sin^2 k_x + (2t_1 \cos k_x + \mu_1)^2} \\
 & \times \sqrt{4\Delta_2^2 k_y^2 + m_2^2}. \quad (37)
 \end{aligned}$$

Finally, we expand the MKC perpendicular Hamiltonian at the vicinity of the critical point, $\mu_1 \sim -2t_1$ and $\mu_2 \sim -2t_2$, with both $k_x, k_y \rightarrow 0$, so that the Dirac Hamiltonian is found to be

$$\begin{aligned}
 H_{D,x,y}(k_x, k_y) = & -m_1 m_2 \Gamma^{zz} - 2m_1 \Delta_2 k_y \Gamma^{zy} + 2\Delta_1 m_2 k_x \Gamma^{yz} \\
 & + 4\Delta_1 \Delta_2 k_x k_y \Gamma^{yy}. \quad (38)
 \end{aligned}$$

Again, from the last expression, the doubly degenerate energy is shown below,

$$E(k_x, k_y) = \pm \sqrt{4\Delta_1^2 k_x^2 + m_1^2} \sqrt{4\Delta_2^2 k_y^2 + m_2^2}. \quad (39)$$

As evident from all the Dirac Hamiltonian energies, the group velocity of the quasiparticles has both x and y components. We illustrate for the last case when both parents are near criticality, when the group velocity turns out to be

$$\mathbf{v}(k_x, k_y) = \pm 4\Delta_1 \Delta_2 (k_y \mathbf{e}_x + k_x \mathbf{e}_y). \quad (40)$$

The velocity field in the \mathbf{k} -space for this case looks like an antivortex structure and may be helpful in creating further exotic phases by stacking a similar Bloch Hamiltonian structure as the MKC perpendicular system with coupling in the z -direction, as done in the case of the KC Bloch Hamiltonian while constructing a Chern insulator.

3. Bulk topology of the perpendicular MKC

As in the case of the parallel MKC, we now characterize the topology of the child Hamiltonian without assuming knowledge of how the child Hamiltonian is constructed from parent Hamiltonians, nor how its topology is determined by topological invariants of the parents. For this reason, we calculate the Wannier spectra for the different topological phases of the perpendicular MKC. For one-dimensional systems, a Wilson loop is expressed as in Eq. (15), but it can be generalized for the two-dimensional Brillouin zone of the perpendicular MKC as the Wilson loop across the k_x BZ for a given k_y and across the k_y BZ for a given k_x . We use the alternative definition of a Wilson loop matrix in terms of the occupied state projectors,

$$\mathcal{W}_{mn} = \langle u_m(\mathbf{k}_0) | \lim_{R \rightarrow \infty} \prod_{i=R}^1 P(\mathbf{k}_i) | u_n(\mathbf{k}_0) \rangle, \quad (41)$$

and we calculate the matrix components for the case with a loop along the k_x BZ for a given k_y , as shown explicitly in

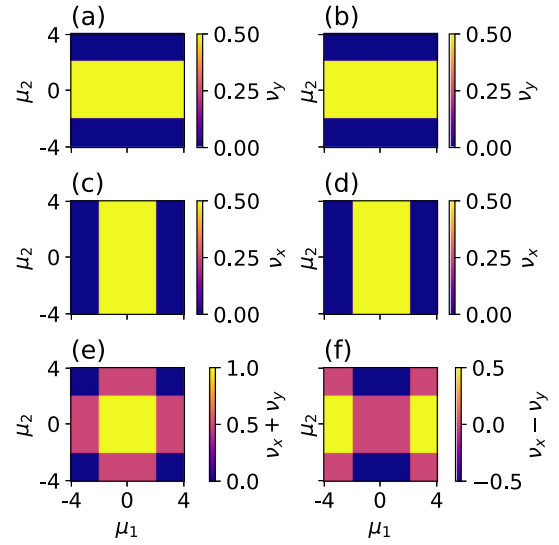


FIG. 16. Wannier spectra $v_{x/y}$ (color bar) for MKC perpendicular system derived from Wilson loop operators, \mathcal{W}_x [(a) and (b)] and \mathcal{W}_y [(c) and (d)], respectively. We also plot $v_x \pm v_y$ in row 3 [(e) and (f)] in the left and right, respectively.

Supplemental Material, Sec. S2 [27] in Eq. S75,

$$\begin{aligned}
 \mathcal{W}_{11} &= \langle v_{1+}(k_{x0}) | \lim_{R \rightarrow \infty} \left[\prod_{i=R}^1 P_{1+}(k_{xi}) \right] | v_{1+}(k_{x0}) \rangle, \\
 \mathcal{W}_{22} &= \langle v_{1-}(k_{x0}) | \lim_{R \rightarrow \infty} \left[\prod_{i=R}^1 P_{1-}(k_{xi}) \right] | v_{1-}(k_{x0}) \rangle, \\
 \mathcal{W}_{12} &= \mathcal{W}_{21} = 0. \quad (42)
 \end{aligned}$$

One can similarly work out the alternative case in which the loop is along the k_y BZ for a given k_x and the final Wannier spectra is given as

$$\begin{aligned}
 v_i &= v_x = v^{(1)} \bmod 1 \quad \text{for BZ along } k_x \text{ and given } k_y, \\
 v_i &= v_y = v^{(2)} \bmod 1 \quad \text{for BZ along } k_y \text{ and given } k_x, \quad (43)
 \end{aligned}$$

where $v^{(j)}$, $j \in \{1, 2\}$ is the Wannier spectra due to the i th parent Hamiltonian.

The topology of two-dimensional phases is then characterized in terms of the *winding* of these two Wilson loops as a function of k_x and k_y , respectively. We find, however, that these two quantities are each constant as a function of k_x or k_y , and we therefore may characterize the topology entirely with $\mathcal{W}(k_x)$ [$\mathcal{W}(k_y)$], with k_x (k_y) fixed and integration over k_y (k_x). We therefore compute Wannier center charge spectra for Wilson loops computed by integrating over k_x (k_y) for each k_y (k_x) and shown in Fig. 16. We find that the spectra exhibit topologically nontrivial Wannier charge center values when one of the parent Hamiltonians is in a topologically nontrivial state. The spectra are topologically trivial when both parents are topologically trivial, but *also when both parents are topological, and the child is also actually topologically nontrivial*. In the regime, when both parents are topological, we have

$(\nu_x, \nu_y) \equiv (0.5, 0.5)$, where $\nu_{x/y}$ refer to the Wannier spectra derived from Wilson loop operators \mathcal{W}_x and \mathcal{W}_y , respectively.

Akin to the parallel MKC, we still have two flavors of chiral symmetries for the perpendicular MKC— $\tau^x \otimes \mathcal{I}$ arising from parent 1 and $\mathcal{I} \otimes \sigma^x$ arising from parent 2. Furthermore, we still possess the unitary symmetry— $\tau^x \sigma^x$ for the perpendicular MKC formed from the combination of the two chiral symmetries. Just like the parallel MKC, one can block-diagonalize the perpendicular MKC in the diagonal basis of the unitary symmetry. This results in two band blocks of the four-band Hamiltonian, which we again denote as component Hamiltonians. These component Hamiltonians are two-band Kitaev systems in 2D with next-nearest-neighbor coupling,

and we define them as follows:

$$H_{\text{MKC},\perp}^c = \frac{1}{2} \sum_k \tilde{c}_{k,1}^\dagger \mathcal{H}_{\perp,1}(\mathbf{k}) \tilde{c}_{k,1} + \frac{1}{2} \sum_k \tilde{c}_{k,2}^\dagger \mathcal{H}_{\perp,2}(\mathbf{k}) \tilde{c}_{k,2},$$

$$(\tilde{c}_{k,1}, \tilde{c}_{k,2})^T = U^\dagger (c_{k,\uparrow}, c_{k,\downarrow}, c_{-k,\uparrow}^\dagger, c_{-k,\downarrow}^\dagger)^T, \quad (44)$$

where

$$\tilde{c}_{k,1} = (\tilde{c}_{k,\uparrow}, \tilde{c}_{-k,\downarrow}^\dagger)^T, \quad \tilde{c}_{k,2} = (\tilde{c}_{k,\downarrow}, \tilde{c}_{-k,\uparrow}^\dagger)^T,$$

$$U = \frac{1}{\sqrt{2}} \begin{pmatrix} 1 & 0 & 0 & 1 \\ 0 & 1 & 1 & 0 \\ 0 & 1 & -1 & 0 \\ 1 & 0 & 0 & -1 \end{pmatrix},$$

$$\begin{aligned} \mathcal{H}_{\perp,1}(k) = & -[2\mu_2 t_1 \cos k_x + 2\mu_1 t_2 \cos k_y + 2(t_1 t_2 + \Delta_1 \Delta_2) \cos(k_x + k_y) + 2(t_1 t_2 - \Delta_1 \Delta_2) \cos(k_x - k_y) + \mu_1 \mu_2] \sigma^z \\ & + [2\mu_2 \Delta_1 \sin k_x + 2\mu_1 \Delta_2 \sin k_y + 2(t_2 \Delta_1 + t_1 \Delta_2) \sin(k_x + k_y) \\ & + 2(t_2 \Delta_1 - t_1 \Delta_2) \sin(k_x - k_y)] \sigma^y = \mathbf{d}_1(k) \cdot \boldsymbol{\sigma}, \end{aligned} \quad (45a)$$

$$\begin{aligned} \mathcal{H}_{\perp,2}(k) = & -[2\mu_2 t_1 \cos k_x + 2\mu_1 t_2 \cos k_y + 2(t_1 t_2 - \Delta_1 \Delta_2) \cos(k_x + k_y) + 2(t_1 t_2 + \Delta_1 \Delta_2) \cos(k_x - k_y) + \mu_1 \mu_2] \sigma^z \\ & + [2\mu_2 \Delta_1 \sin k_x - 2\mu_1 \Delta_2 \sin k_y + 2(t_2 \Delta_1 - t_1 \Delta_2) \sin(k_x + k_y) + 2(t_2 \Delta_1 + t_1 \Delta_2) \sin(k_x - k_y)] \sigma^y = \mathbf{d}_2(k) \cdot \boldsymbol{\sigma}, \end{aligned} \quad (45b)$$

It has been shown [31] that for 2D Kitaev chains, the topology is characterized by vortices in the Bloch vector field over k_x and k_y . However, we instead plot how the Bloch vector winds in $k_x(k_y)$ as we fix $k_y(k_x)$ to highlight the vortex structure clearly. Through this, we illustrate that it is possible to identify the bulk topology as well as relate it to the number of the MZMs along a certain edge. We will work with the matrices, $\mathbf{d}_1(k_x, k_y)$ and $\mathbf{d}_2(k_x, k_y)$ with PBC in both the x - and y -directions so that the matrix element $d_{1,2}(n, m)$ is given by $k_x = \frac{2\pi n}{L_x}$ and $k_y = \frac{2\pi m}{L_y}$ for $n \in \{0, \dots, L_x\}$ and $m \in \{0, \dots, L_y\}$, with L_x and L_y being the number of sites in the x - and y -directions, respectively ($L_x + 1$ or $L_y + 1$ values are used for n and m , respectively, to close the curve; only the first L_x and L_y values are considered for discussion). We then plot the n th row of $d_{1,y}$ versus the n th row of $d_{1,z}$ and similarly for $d_{2,y}$ and $d_{2,z}$. Since we have varying k_x with fixed k_y along a given row, we obtain the MZMs along the edge in the y -direction in the form of L_y loops. These loops enclose the origin if $\mu_1 < 2t_1$; touch the origin if $\mu_1 = 2t_1$ and do not contain the origin if $\mu_1 > 2t_1$. This is illustrated for $L_x = 100$ and $L_y = 6$ in Figs. 17(a), 17(c), and 17(e). In addition, for the case $t_{1,2} = \Delta_{1,2}$, where the closed curve is a circle in the two-band KC, we see that the polygon created by joining the centers of the six circles also encloses the origin if $\mu_2 < 2t_2$ and intersects the origin when $\mu_2 = 2t_2$. In the latter case, due to the discreteness of the lattice, the intersection of the origin is only guaranteed if the chain is even; when the chain is odd, it is possible that there is no critical point in which the loop moves through the origin.

To analyze the appearance of MZMs in the perpendicular direction, we investigate the winding of the m th column of $d_{1,y}$ versus the m th column of $d_{1,z}$ and similarly for $d_{2,y}$ and $d_{2,z}$.

The plot for $L_x = 8$ and $L_y = 100$ is displayed in Figs. 17(b), 17(d), and 17(f). Here for each fixed k_x there is a closed curve that encircles the origin. For the parameter region $\mu_2 < 2t_2$, these eight loops correspond to the eight MZMs along the edges in the x -direction.

The locus of the curves is calculated when $t_1 = \Delta_1$ for varying k_x and constant k_y , as follows (a detailed calculation is in the Supplemental Material, Sec. S3 [27]):

$$\begin{aligned} 2t_1 \sqrt{M_2^2 + R_2^2} = & (\cos \theta d_{1,y} + \sin \theta d_{1,z})^2 \\ & + (\cos \theta d_{1,z} - \sin \theta d_{1,y} + \mu_1 \sqrt{M_2^2 + R_2^2})^2, \end{aligned} \quad (46)$$

where we denote $M_2 = \mu_2 + 2t_2 \cos k_y$, $R_2 = 2\Delta_2 \sin k_y$, and $\tan \theta = \frac{R_2}{M_2}$. The θ presented here is interpreted as the Bloch angle of the second parent Hamiltonian. Upon calculation, one sees that for each fixed k_y the locus is a circle centered at a vertex of an L_y -sided polygon, at a distance proportional to the k_y energy contour. Finally, the radius of each locus at a vertex is also proportional to the energy contour defined by the fixed k_y . Through this geometric interpretation, we may see that the origin is enclosed by the loci at fixed k_y when the radii of the loci are larger than the distance of the center of each loci from the origin. Consequently, the ratio between these two lengths provides the expected topological region $|\mu_1| < 2t_1$.

Here, the difference in the winding number characterization between the MKC parallel system and the MKC perpendicular system is explicit. For the MKC parallel system, Fig. 3 has shown that the winding number is a combination of the winding numbers corresponding to the parents.

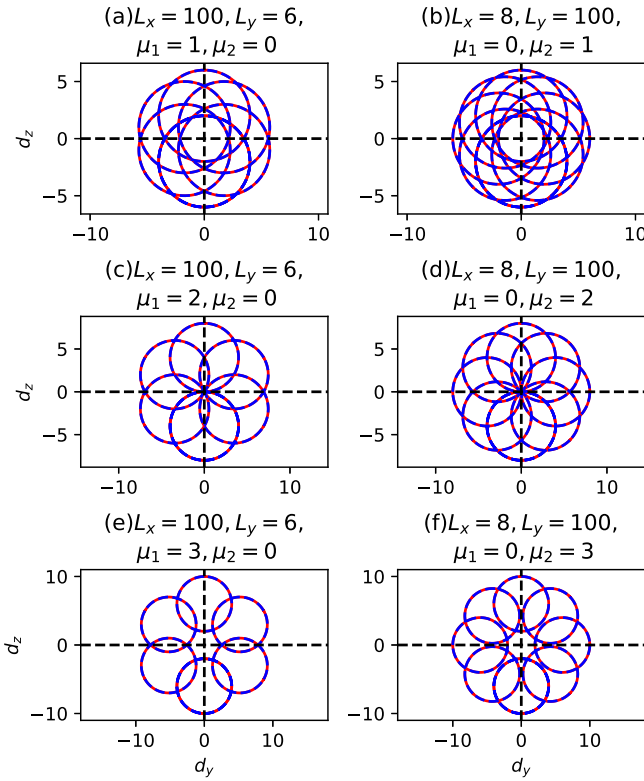


FIG. 17. Winding from the Bloch vectors $(d_{1,y}, d_{1,z})$ (red) and $(d_{2,y}, d_{2,z})$ (blue dashed) with PBC along both the x and y directions. Parts (a), (c), and (e) are the closed curves due to PBC $L_x = 100$ and $L_y = 6$, where the six circles show the situation along the edge in the y -direction for (a) $\mu_1 = 1, \mu_2 = 0$ (MZMs present), (c) $\mu_1 = 2, \mu_2 = 0$ (critical), and (e) $\mu_1 = 3, \mu_2 = 0$ (trivial along the y edge), respectively. Similarly, (b), (d), and (f) are the closed curves due to PBC $L_x = 8$ and $L_y = 100$, where the eight circles show the situation along the edge in the x -direction for (b) $\mu_1 = 0, \mu_2 = 1$ (MZMs present), (d) $\mu_1 = 0, \mu_2 = 2$ (critical), and (f) $\mu_1 = 0, \mu_2 = 3$ (trivial along the x edge). The Bloch vectors \mathbf{d}_1 and \mathbf{d}_2 overlap so that the situation is similar for both the component Hamiltonians. All the cases assume $t_1 = 1 = t_2 = \Delta_1 = \Delta_2$.

Therefore, even if at least one of the parent systems is topological, the sum of the absolute value of winding derived from both systems adds up to two. However, in the MKC perpendicular system, the winding curves of both component Hamiltonians are equivalent, such that the component Hamiltonians always have equal winding. The difference here is in the nature of the winding when one varies the k_x direction compared to the k_y direction, keeping the perpendicular momenta constant for a given curve.

We will follow our analysis of the bulk topology in the MKC perpendicular system with a systematic analysis of the edge states in the real-space Hamiltonian in the next section. We will demonstrate that the relevant bulk boundary

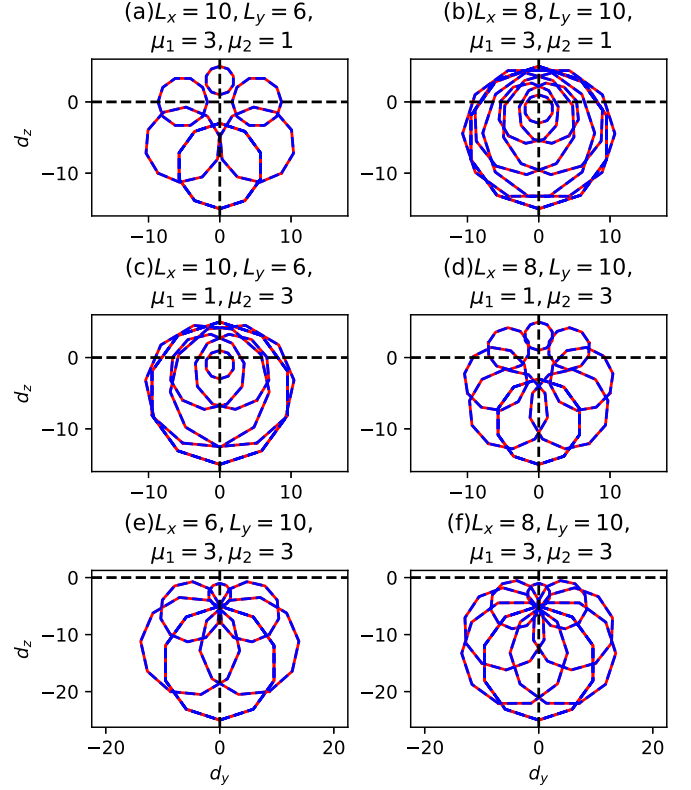


FIG. 18. Winding from the Bloch vectors $(d_{1,y}, d_{1,z})$ (red) and $(d_{2,y}, d_{2,z})$ (blue dashed) with PBC along both x and y directions. We see more clearly the modulation of the winding curves in one direction due to its perpendicular part, and the curves are actually polygons if both edges are smaller. But since the winding depends on the bulk, this should not change the final outcome. Parts (a), (c), and (e) are the closed curves due to PBC $L_x = 10$ and $L_y = 6$, where the six circles show the situation along the edge in the y -direction for (a) $\mu_1 = 3, \mu_2 = 1$ (MZMs along x , trivial along y), (c) $\mu_1 = 1, \mu_2 = 3$ (MZMs along y , trivial along x), and (e) $\mu_1 = 3, \mu_2 = 3$ (trivial along both edges), respectively. Similarly, (b), (d), and (f) are the closed curves due to PBC $L_x = 8$ and $L_y = 10$, where the eight circles show the situation along the edge in the x -direction for (b) $\mu_1 = 3, \mu_2 = 1$ (MZMs along x , trivial along y), (d) $\mu_1 = 1, \mu_2 = 3$ (MZMs along y , trivial along x), and (f) $\mu_1 = 3, \mu_2 = 3$ (trivial along both edges). The Bloch vectors \mathbf{d}_1 and \mathbf{d}_2 overlap so that the situation is similar for both the component Hamiltonians. All the cases assume $t_1 = 1 = t_2 = \Delta_1 = \Delta_2$.

correspondence directly maps to the number and nature of the windings we have shown in Figs. 17 and 18.

B. Perpendicular MKC Hamiltonian in real space

For convenience again, we redefine our notation from Sec. III B, $\gamma_{j,+} = (\gamma_{j,+,\uparrow}, \gamma_{j,+,\downarrow})$ and $\gamma_{j,-} = (\gamma_{j,-,\uparrow}, \gamma_{j,-,\downarrow})^T$. Then one can express the MKC Hamiltonian in the case of

perpendicular parents as follows in real space:

$$\begin{aligned}
H_{\text{MKC},\perp}^c = & \frac{1}{2} \sum_{i,j} -(t_1 - \Delta_1) i \gamma_{i,j,+} (t_2 \sigma^z - i \Delta_2 \sigma^y) \gamma_{i+1,j+1,-} - (t_1 + \Delta_1) i \gamma_{i+1,j+1,+} (t_2 \sigma^z + i \Delta_2 \sigma^y) \gamma_{i,j,-} \\
& - (t_1 - \Delta_1) i \gamma_{i,j,+} (t_2 \sigma^z + i \Delta_2 \sigma^y) \gamma_{i+1,j-1,-} - (t_1 + \Delta_1) i \gamma_{i+1,j-1,+} (t_2 \sigma^z - i \Delta_2 \sigma^y) \gamma_{i,j,-} \\
& - \mu_2 (t_1 - \Delta_1) i \gamma_{i,j,+} \sigma^z \gamma_{i+1,j,-} - \mu_2 (t_1 + \Delta_1) i \gamma_{i+1,j,+} \sigma^z \gamma_{i,j,-}, \\
& - \mu_1 i \gamma_{i,j,+} (t_2 \sigma^z - i \Delta_2 \sigma^y) \gamma_{i,j+1,-} - \mu_1 i \gamma_{i+1,+} (t_2 \sigma^z + i \Delta_2 \sigma^y) \gamma_{i,j,-} - \mu_1 \mu_2 i \gamma_{i,j,+} \sigma^z \gamma_{i,j,-}. \tag{47}
\end{aligned}$$

We execute the same similarity transformation as done in the MKC parallel case, which changes the Hamiltonian expression to

$$\begin{aligned}
H_{\text{MKC},\perp}^c = & \frac{i}{2} \sum_{i,j} [-(t_1 - \Delta_1)(t_2 - \Delta_2) \tilde{\gamma}_{i,j,\uparrow,+} \tilde{\gamma}_{i+1,j+1,\downarrow,-} - (t_1 + \Delta_1)(t_2 + \Delta_2) \tilde{\gamma}_{i+1,j+1,\uparrow,+} \tilde{\gamma}_{i,j,\downarrow,-} \\
& - (t_1 - \Delta_1)(t_2 + \Delta_2) \tilde{\gamma}_{i,j,\uparrow,+} \tilde{\gamma}_{i+1,j-1,\downarrow,-} - (t_1 + \Delta_1)(t_2 - \Delta_2) \tilde{\gamma}_{i+1,j-1,\uparrow,+} \tilde{\gamma}_{i,j,\downarrow,-} - \mu_2 (t_1 - \Delta_1) \tilde{\gamma}_{i,j,\uparrow,+} \tilde{\gamma}_{i+1,j,\downarrow,-} \\
& - \mu_2 (t_1 + \Delta_1) \tilde{\gamma}_{i+1,j,\uparrow,+} \tilde{\gamma}_{i,j,\downarrow,-} - \mu_1 (t_2 - \Delta_2) \tilde{\gamma}_{i,j,\uparrow,+} \tilde{\gamma}_{i+1,j+1,\downarrow,-} - \mu_1 (t_2 + \Delta_2) \tilde{\gamma}_{i+1,j+1,\uparrow,+} \tilde{\gamma}_{i,j,\downarrow,-} \\
& - \mu_1 \mu_2 \tilde{\gamma}_{i,j,\uparrow,+} \tilde{\gamma}_{i,j,\downarrow,-}] + \frac{i}{2} \sum_{i,j} [-(t_1 - \Delta_1)(t_2 + \Delta_2) \tilde{\gamma}_{i,j,\downarrow,+} \tilde{\gamma}_{i+1,j+1,\uparrow,-} - (t_1 + \Delta_1)(t_2 - \Delta_2) \tilde{\gamma}_{i+1,j+1,\downarrow,+} \tilde{\gamma}_{i,j,\uparrow,-} \\
& - (t_1 - \Delta_1)(t_2 - \Delta_2) \tilde{\gamma}_{i,j,\downarrow,+} \tilde{\gamma}_{i+1,j-1,\uparrow,-} - (t_1 + \Delta_1)(t_2 + \Delta_2) \tilde{\gamma}_{i+1,j-1,\downarrow,+} \tilde{\gamma}_{i,j,\uparrow,-} - \mu_2 (t_1 - \Delta_1) \tilde{\gamma}_{i,j,\downarrow,+} \tilde{\gamma}_{i+1,j,\uparrow,-} \\
& - \mu_2 (t_1 + \Delta_1) \tilde{\gamma}_{i+1,j,\downarrow,+} \tilde{\gamma}_{i,j,\uparrow,-} - \mu_1 (t_2 + \Delta_2) \tilde{\gamma}_{i,j,\downarrow,+} \tilde{\gamma}_{i+1,j+1,\uparrow,-} - \mu_1 (t_2 - \Delta_2) \tilde{\gamma}_{i+1,j+1,\downarrow,+} \tilde{\gamma}_{i,j,\uparrow,-} - \mu_1 \mu_2 \tilde{\gamma}_{i,j,\downarrow,+} \tilde{\gamma}_{i,j,\uparrow,-}], \\
= & H_{1,\perp} + H_{2,\perp}. \tag{48}
\end{aligned}$$

Based on the diagram shown in Fig. 19, it is possible to deduce the possibility and placement of Majorana zero modes even if the system has finite length and width. We introduce all the interactions present with respect to one site in Figs. 19(a) and 19(b) for the component Hamiltonians $H_{\perp,1}$ and $H_{\perp,2}$, and then we prioritize the case for which $t_{1,2} = \Delta_{1,2}$ [Figs. 19(c) and 19(d)], where we find the Majorana zero mode parent Hamiltonian for suitable $\mu_{1,2}$.

Case 1. We first look at the case when parent 1 is topological, with $\mu_1 = 0$, while parent 2 is trivial with $\mu_2 > 2t_2$. Figures 19(f) and 19(g) show that both $H_{1,\perp}$ and $H_{2,\perp}$ have Majorana zero modes running along both the edges parallel to the y -axis of the square lattice. Numerical simulation in Fig. 20(a) agrees with this analytical calculation. The schematic diagram further illustrates that the states localized along each edge are twofold-degenerate, as each component Hamiltonian in Eq. (48) contributes a Majorana edge state.

Case 2. Now, we consider parent 2 in the topological phase, with $\mu_2 = 0$, and parent 1 in the trivial phase by requiring that $\mu_1 > 2t_1$. From Figs. 19(e) and 19(f) for $H_{1,\perp}$ and $H_{2,\perp}$, respectively, one observes Majorana zero modes in the square lattice along the two edges parallel to the x -axis. Again, each Hamiltonian component contributes one Majorana state localized at each edge, yielding a twofold degeneracy of the Majorana zero modes. Numerical simulations in Fig. 20(d) are consistent with our analytical expressions.

Case 3. Finally, we consider the case in which each parent is topologically nontrivial. This is illustrated in Figs. 19(i) and 19(j) and Figs. 19(k) and 19(l) for $\mu_1 = 0$, $\mu_2 < 2t_2$ and $\mu_1 < 2t_1$, $\mu_2 = 0$, respectively. Notice the alternatively connected dashed and solid lines, which indicates a number of decoupled Kitaev chains. The conditions $\mu_1 < 2t_1$ in Figs. 19(i) and 19(l) and $\mu_2 < 2t_2$ in Figs. 19(j) and 19(k) then naturally imply that

each of the decoupled Kitaev chains is topologically nontrivial and hence has a Majorana zero mode at the edges. The interesting fact to notice, however, is that the whole perimeter of the finite-size system now has Majorana zero modes with twofold degeneracy (each of $H_{1,\perp}$ and $H_{2,\perp}$ provides one MZM). This also agrees with our numerical simulation in Figs. 20(g) and 20(h). In addition, the corners seem to host three degenerate Majoranas. This may indicate the presence of higher-order [32] topological edge modes, but we defer this discussion to a later article.

Ultimately, these results validate our analysis of the bulk topology from Figs. 17 and 18. In Case 3, when both parents are topological and the child has dimensions $L_x \times L_y$, we have L_x pairs of Majoranas along the edge parallel to y and L_y pairs of Majoranas parallel to x . This number is equal to the number of circles enclosing the origin in Figs. 17(a) and 17(b), and the MZMs directly correspond to the winding derived from these circles. Again from Case 1 and Case 2, the Majorana pairs are localized along edges parallel to the direction along which the nontopological parent lies. The number of such Majorana pairs maps to the number of circles or polygons with the winding one in Fig. 18(b) which is the value of L_x and in Fig. 18(c) the value being L_y —this directly provides the bulk-boundary correspondence in Cases 1 and 2. There exists no winding for the circles or polygons in Figs. 18(a) and 18(d), which again confirms our real-space analysis—there exist no Majorana pairs along the direction of the topological parent. The topology derived from each parent seems to be disconnected in the MKC perpendicular system unlike the MKC parallel system, which our winding number and real space confirms. Moreover, the Wilson loop analysis, which seemed to be unreliable in the MKC parallel case, agrees with the winding number analysis in the MKC perpendicular case as shown from Fig. 16.

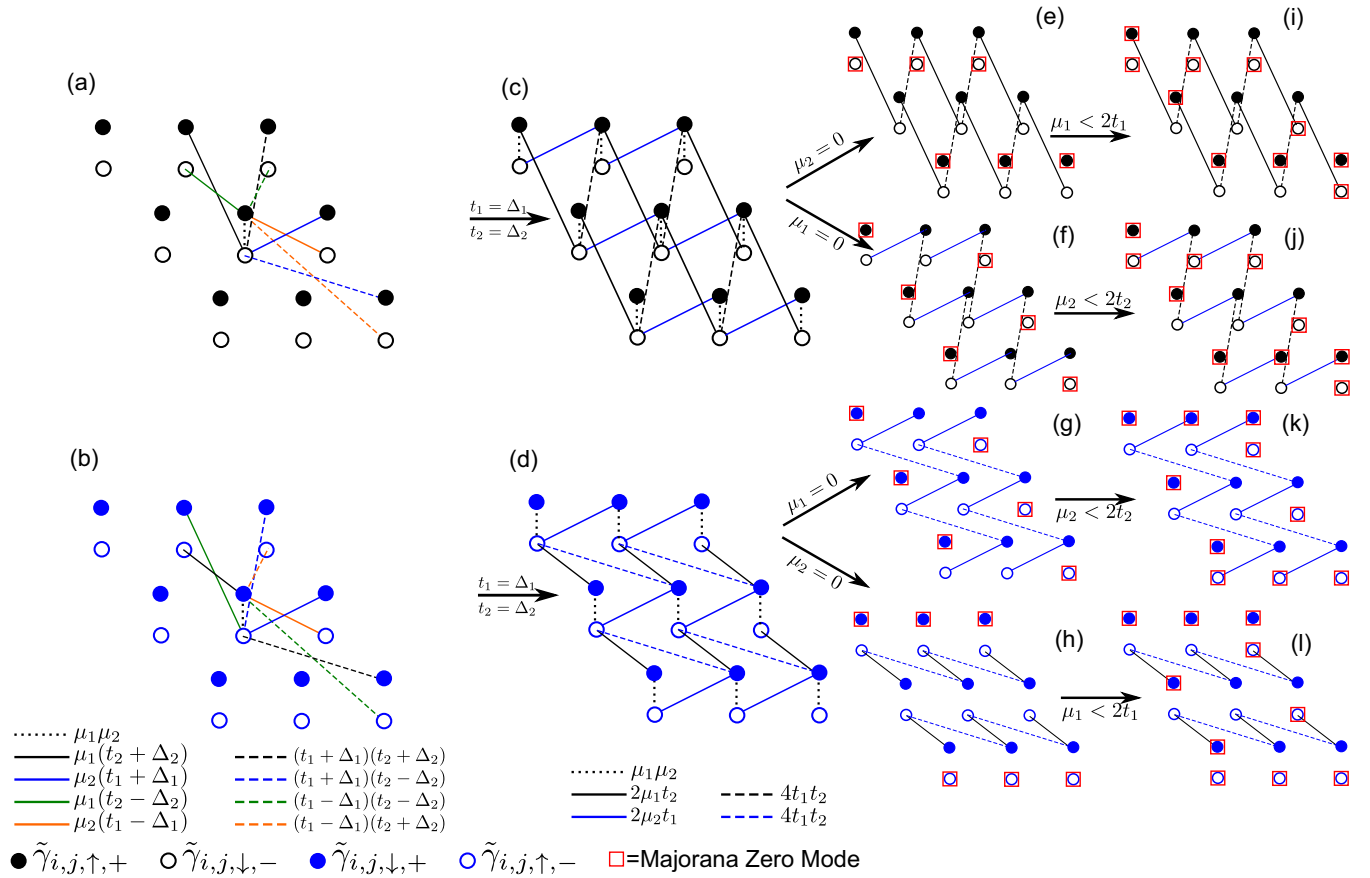


FIG. 19. Schematic representation of the MKC perpendicular system in terms of Majorana fermionic interactions using the color scheme mentioned in the legends at the bottom left corner of the figure, (a) for $t_1 = \Delta_1$ and (b) for $t_1 = \Delta_1$ and $\mu_1 = \mu_2 = 0$. One can see that for translational symmetry in the y -direction, one gets Majorana edge modes along the whole y -axis for a finite slab in the x -direction, as discussed beforehand.

1. Edge states of the MKC perpendicular system from the component Hamiltonians and entanglement

Having convinced ourselves about the bulk-boundary correspondence in the MKC perpendicular system, next we analytically derive the expressions for the edges from the component Bloch Hamiltonians in Eqs. (45a) and (45b). Here we assume OBC in both the x and y directions so that one can implement localization in both directions as $k_x \rightarrow iq_x$ and $k_y \rightarrow iq_y$, resulting in the conditions

$$\begin{aligned}
 & [(2t_1 \cosh q_x + \mu_1) \pm 2\Delta_1 \sinh q_x] \\
 & \times [(2t_2 \cosh q_y + \mu_2) \pm 2\Delta_2 \sinh q_y] = 0, \quad (49a)
 \end{aligned}$$

$$\begin{aligned}
 & [(2t_1 \cosh q_x + \mu_1) \pm 2\Delta_1 \sinh q_x] \\
 & \times [(2t_2 \cosh q_y + \mu_2) \mp 2\Delta_2 \sinh q_y] = 0 \quad (49b)
 \end{aligned}$$

on the decay constants. We calculate these relations explicitly from $H_{\perp,1}$ and $H_{\perp,2}$, respectively, in Sec. S1 B of the Supplemental Material [27]. We assume a semi-infinite 2D system with the wave function for the edge states vanishing at $x = 0$ for any y and $y = 0$ for any x . Taking a separable ansatz, and inputting the boundary conditions, $\Psi(j, 0) = \Psi(0, l) = 0$, we have, for example, in $H_{\perp,1}$ for the sign (+, +),

$$\Psi(j, l) \sim [p_{1,+}^j - p_{1,-}^j][s_{1,+}^l - s_{1,-}^l], \quad (50)$$

and in $H_{\perp,2}$ for the sign (+, -),

$$\Psi(j, l) \sim [p_{1,+}^j - p_{1,-}^j][s_{2,+}^l - s_{2,-}^l]. \quad (51)$$

Here we denote $p_{1,\pm} = \frac{-\mu_1 \pm \sqrt{\mu_1^2 - 4(t_1^2 - \Delta_1^2)}}{2(t_1 + \Delta_1)}$, $p_{2,\pm} = \frac{-\mu_1 \pm \sqrt{\mu_1^2 - 4(t_1^2 - \Delta_1^2)}}{2(t_1 - \Delta_1)}$, $s_{1,\pm} = \frac{-\mu_2 \pm \sqrt{\mu_2^2 - 4(t_2^2 - \Delta_2^2)}}{2(t_2 + \Delta_2)}$, and $s_{2,\pm} = \frac{-\mu_2 \pm \sqrt{\mu_2^2 - 4(t_2^2 - \Delta_2^2)}}{2(t_2 - \Delta_2)}$.

As in the case of the MKC parallel system, the Majorana zero modes (MZMs) can be shown to be entangled or product states based on the topological nature of the parent Hamiltonians or the boundary conditions one imposes. Unlike the MKC parallel system, the MKC perpendicular system has the added advantage that even if both parents are topological, it is possible to change the entanglement by considering cylindrical geometries. To show this, let us consider the condition Eq. (49a) for $\text{sgn}(t_i) = \text{sgn}(\Delta_i)$, $i \in \{1, 2\}$,

$$\begin{aligned}
 & [(2t_1 \cosh q_x + \mu_1) - 2\Delta_1 \sinh q_x] \\
 & \times [(2t_2 \cosh q_y + \mu_2) - 2\Delta_2 \sinh q_y] = 0. \quad (52)
 \end{aligned}$$

If there exists OBC along both the x and y directions and both the parents are topological, we have, $2t_1 \cosh q_x + \mu_1 = 2\Delta_1 \sinh q_x$ and $2t_2 \cosh q_y + \mu_2 = 2\Delta_2 \sinh q_y$, which implies that $\mathcal{H}_{\perp,2}$ vanishes as shown in Supplemental Material

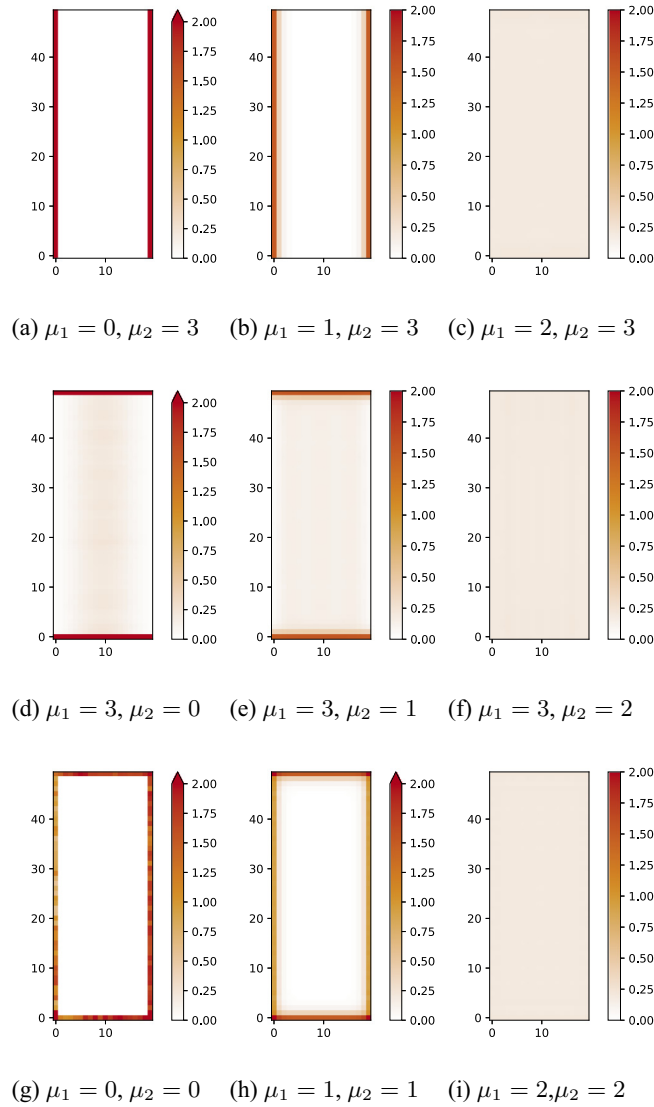


FIG. 20. Density plots for zero-energy Majorana modes for a finite 20×50 slab of MKC perpendicular system at different values of μ_1 and μ_2 . All the systems have $t_1 = t_2 = 1$ and $\Delta_1 = \Delta_2 = 1$.

[27], Sec. S1 B. We note that we are actually working in the full basis of the MKC perpendicular system, given by the four degrees of freedom, $(\tilde{c}_{k,\uparrow}, \tilde{c}_{k,\downarrow}, \tilde{c}_{-k,\uparrow}^\dagger, \tilde{c}_{-k,\downarrow}^\dagger)^T$, which combines the degrees of freedom of the two component Hamiltonians. In this basis, the null eigenvectors derived from $\mathcal{H}_{\perp,1}(iq_x, iq_y)$ are given as

$$|\Psi\rangle_{\text{MZM}} = \left\{ \frac{1}{\sqrt{2}}(|00\rangle - |11\rangle), |01\rangle, |10\rangle \right\}, \quad (53)$$

where $|0\rangle = (1, 0)^T$ and $|1\rangle = (0, 1)^T$.

Now, say if *parent 1 is topological while parent 2 is trivial while we retain OBC in both x and y directions*, we must only satisfy the condition, $2t_1 \cosh q_x + \mu_1 = 2\Delta_1 \sinh q_x$. Again from calculations shown in Supplemental Material, Sec. S1 B [27], the null eigenvectors in the full basis with four degrees of freedom are shown to be

$$|\Psi\rangle_{\text{MZM}} = \left\{ \frac{1}{\sqrt{2}}(|00\rangle - |11\rangle), \frac{1}{\sqrt{2}}(|01\rangle - |10\rangle) \right\}. \quad (54)$$

One must note that the above eigenvectors are also valid if the *y-direction is unopened or in PBC so that the topological nature of the second parent does not matter*. Then only the condition $2t_1 \cosh q_x + \mu_1 = 2\Delta_1 \sinh q$ holds.

Consequently, in contrast to the MKC parallel system, the entanglement between maximally entangled Bell states and product states can be controlled completely, not only via the topological nature of the parents but also the geometry of the sample. We provide a small table (Table II) showing all the possible MZM eigenvectors under various parent topology and boundary conditions. The table lists only the MZM eigenvector at edges $x = 0$ and $y = 0$. The eigenvectors at the other edges can be found by changing $\frac{\text{sgn}(t_i)}{\text{sgn}(\Delta_i)}$ from $+$ to $-$ and *vice versa* for both parents. We will recover a total of four eigenvectors with two common eigenvectors for both signs when both parents are topological. Thus, the MZMs obtained in this case have a similar entanglement structure as in the parallel case.

2. Parallel quantum gates without braiding

The MZMs of the perpendicular MKC system can also be entangled states and separable two-qubit states via variation of the system parameters at a given parity. In this case, however, there is the potential to perform parallel gate operations: since the number of MZM pairs that the perpendicular system has is proportional to the perimeter of the system (when there are open boundary conditions in each direction), it is possible to carry out CNOT operations simultaneously on a large number of MZM pairs. The full potential for universal quantum computation schemes by manipulating multiplicative topological phases in combination with this potential for parallelized gate operations warrants further investigation, but this is beyond the scope of this work.

C. Finite MKC perpendicular system with open boundary conditions

To begin characterizing the perpendicular MKC with open boundary conditions, we consider a slab geometry, with open boundary conditions in the \hat{x} -direction and periodic in the \hat{y} -direction. We first characterize the spectral properties of the system with these boundary conditions, finding evidence of additional topologically protected boundary modes under these conditions. We then characterize these topologically protected boundary states in greater detail focusing on localization of the states. We support numerical findings with additional analytical characterization of the boundary modes in a variety of limiting cases.

1. Spectral dependence on the chemical potential

We begin by considering the slab geometry with $L_x = 80$, which is much larger than the coherence length of the edge states. These results are shown in Fig. 21.

We see along the cut in the phase diagram $\mu_1 = \mu_2$ the existence of zero-energy states, in fact these are actually dispersionless as expected in the schematic diagram Fig. 19. Furthermore, this numerically verifies what we would expect from the bulk topology.

TABLE II. Eigenvectors of the MKC perpendicular system for different topological characterizations of the two parent systems, ratio of signs of t_i and Δ_i , $i \in \{1, 2\}$, and boundary conditions.

Parent 1			Parent 2			MZM eigenvectors
Phase	$\frac{\text{sgn}(t_1)}{\text{sgn}(\Delta_1)}$	x -BC	Phase	$\frac{\text{sgn}(t_1)}{\text{sgn}(\Delta_1)}$	y -BC	
topo	+	OBC	topo	+	OBC	$\{\frac{1}{\sqrt{2}}(00\rangle - 11\rangle), 01\rangle, 10\rangle\}$
	+	OBC		-	OBC	$\{\frac{1}{\sqrt{2}}(01\rangle - 10\rangle), 00\rangle, 11\rangle\}$
	-	OBC		+	OBC	$\{\frac{1}{\sqrt{2}}(01\rangle + 10\rangle), 00\rangle, 11\rangle\}$
	-	OBC		-	OBC	$\{\frac{1}{\sqrt{2}}(00\rangle + 11\rangle), 01\rangle, 10\rangle\}$
topo	+	OBC	topo	+, -	PBC	$\{\frac{1}{\sqrt{2}}(00\rangle - 11\rangle), \frac{1}{\sqrt{2}}(01\rangle - 10\rangle)\}$
	-	OBC		+, -	PBC	$\{\frac{1}{\sqrt{2}}(00\rangle + 11\rangle), \frac{1}{\sqrt{2}}(01\rangle + 10\rangle)\}$
	+, -	PBC		+	OBC	$\{\frac{1}{\sqrt{2}}(00\rangle - 11\rangle), \frac{1}{\sqrt{2}}(01\rangle + 10\rangle)\}$
	+, -	PBC		-	OBC	$\{\frac{1}{\sqrt{2}}(00\rangle + 11\rangle), \frac{1}{\sqrt{2}}(01\rangle - 10\rangle)\}$
topo	+	OBC	triv			$\{\frac{1}{\sqrt{2}}(00\rangle - 11\rangle), \frac{1}{\sqrt{2}}(01\rangle - 10\rangle)\}$
	-	OBC				$\{\frac{1}{\sqrt{2}}(00\rangle + 11\rangle), \frac{1}{\sqrt{2}}(01\rangle + 10\rangle)\}$
triv			topo	+	OBC	$\{\frac{1}{\sqrt{2}}(00\rangle - 11\rangle), \frac{1}{\sqrt{2}}(01\rangle + 10\rangle)\}$
				-	OBC	$\{\frac{1}{\sqrt{2}}(00\rangle + 11\rangle), \frac{1}{\sqrt{2}}(01\rangle - 10\rangle)\}$

2. Analytical theory for finite size MKC perpendicular edge states

We consider now a fully open geometry, therefore boundary conditions at $x = L_x + 1$ and $y = L_y + 1$ enforced on the edge state expressions in Eqs. (50) and (51) stipulate that

$$\begin{aligned} \mu_1 &= 2\sqrt{t_1^2 - \Delta_1^2} \cos \frac{n_x \pi}{L_x + 1}, \quad n_x \in \{1, \dots, L_x\}, \\ \mu_2 &= 2\sqrt{t_2^2 - \Delta_2^2} \cos \frac{n_y \pi}{L_y + 1}, \quad n_y \in \{1, \dots, L_y\}. \end{aligned} \quad (55)$$

Henceforth, the plot of energy E versus $\mu_1 = \mu_2 = \mu$ should include a total of $L_x \times L_y$ gapless points, with the gapless points due to $\mu_1(\mu_2)$ being $L_y(L_x)$ -degenerate [degenerate by the number of sites along the $y(x)$ -edge] as observed in Fig. 22. As with the MKC parallel, the existence of bubblelike features is a result of the hybridization of edge states when the

system size is comparable to the correlation length of the edge states.

V. DISCUSSION AND CONCLUSION

In this work, we introduce multiplicative topological phases of matter realizing unpaired Majorana zero modes. We find that the recently introduced multiplicative topological phases [12] realize such zero modes through bulk-boundary correspondence, specifically considering a canonical Hamiltonian for realizing such multiplicative topological phases consisting of a symmetry-protected tensor product of two Kitaev chain Hamiltonians. While considerable important work currently focuses on smoking-gun experimental

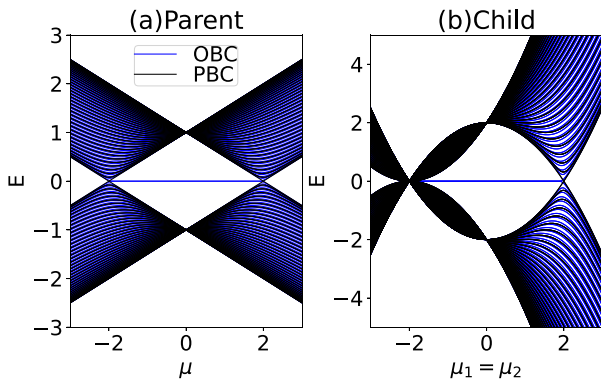


FIG. 21. Slab spectra with $L_x = 80$ for OBC along the x direction (black) and PBC along the y direction (blue) for (a) parent KC with $t = 1 = \Delta$ vs μ , and (b) child MKC perpendicular with $t_1 = t_2 = 1 = \Delta_1 = \Delta_2$ and $k_y = 0$ vs $\mu_1 = \mu_2$.

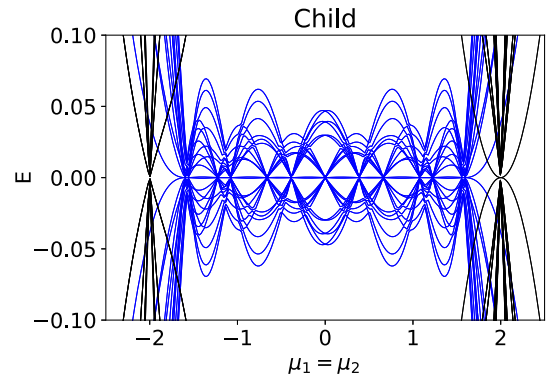


FIG. 22. Spectrum E vs $\mu_1 = \mu_2$ for OBC (blue) and PBC (black) along both the x and y directions with $L_x = 6$ and $L_y = 7$ for $t_1 = t_2 = 1$ and $\Delta_1 = \Delta_2 = 0.5$. We see six gapless points corresponding to OBC along x with sevenfold degeneracy, and seven gapless points corresponding to OBC along y with sixfold degeneracy.

confirmation of unpaired Majorana zero modes and individual topological qubits in experiment, it remains important to identify practical platforms for scalable topological quantum computers. Results discussed here are relevant to realizing such scalable systems of many topological qubits, given that multiplicative Majorana zero modes are individual states composed of multiple symmetry-protected unpaired Majorana zero modes. Additionally, results here indicate there are opportunities for controlled introduction of entanglement between degrees of freedom derived from both parents in the Majorana eigenvectors, potentially useful for performing gate operations of topological quantum computation schemes.

We demonstrate the richness of multiplicative topological phases by constructing one-dimensional *but also two-dimensional* multiplicative Kitaev chain models capable of realizing myriad topologically nontrivial phases. These models consist of either two parent Kitaev chain Hamiltonians that depend on the same momentum component, or perpendicular momentum components, combined in a symmetry-protected, tensor product construction. We lay the groundwork for studying these systems by characterizing bulk topology and corresponding topologically protected boundary states, focusing on the dependence of the resultant multiplicative topological phases on the topology of the parents.

We characterize the bulk of multiplicative Kitaev chains first by demonstrating that eigenvalues of the bulk spectrum are products of the eigenvalues of the parent Kitaev chain bulk spectra, indicating topological phases of the child are stable up to gap-closing of either parent. We also explore characterization of multiplicative topology in the bulk, and we find that Wilson loop spectra successfully characterize some multiplicative topological phases, but they can also indicate trivial topology in the case when each parent is topologically nontrivial. We show, however, that it is possible to decompose the MKC into chiral subsectors to more fully characterize the topology under certain conditions. This exploits the fact that the degrees of freedom of these Hamiltonians are symmetry-constrained, locking together into pseudospins yielding winding numbers that successfully characterize all topologically nontrivial states realized through different combinations of trivial and nontrivial parents considered here. Fully characterizing multiplicative topological phases, however, is an important issue to explore in future works.

Topologically protected boundary states possible for the multiplicative Kitaev chain Hamiltonians are varied. We consider child Hamiltonians, which can be block-diagonalized into chiral subsectors. Based on the topology of the parents, the MZMs of the child may possess either a tensor product or maximally entangled Bell state structure. We characterize

the topology of the child chiral subsectors in the bulk by computing winding numbers for the parallel case, which seem to possess an algebra as one might infer from the addition of angular momentum. We find a relationship between the winding numbers of the child chiral subsectors in the case of two parallel parent Kitaev chains. Schematically, from real-space Hamiltonian expressions, we show that for suitable parametric conditions, MZMs are localized at the outermost and second outermost sites for the 1D (parallel) case or along two or four edges for the 2D (perpendicular) case.

Similarly, we illustrate a winding number calculation for the perpendicular case which accurately reflects the number of MZMs and the edge along which they are localized. A quantization condition for the existence of topologically protected boundary modes in finite-size MKC systems has also been obtained, and we have shown that it agrees with our numerical results for one of the simpler cases. More complicated cases may still be studied, such as one example in Sec. S1 A of the Supplemental Material [27]. This shows that a topologically protected, multiplicative Majorana zero mode of the child MKC, in both the parallel and the perpendicular case, is not just a tensor product of parent Hamiltonian states in general. Instead, they can more generally possess emergent properties evident in their localization, i.e., entanglement and topological robustness.

Future work will explore topological characterization in systems with lower symmetry, for which the multiplicative Majorana zero modes are expected to take more general forms, as well as control of the entanglement properties, which hold great promise for developing more robust and versatile topological quantum computation schemes. This could include further study of the potential for braiding schemes, with the degenerate manifold of zero-energy states, when each parent is topologically non-trivial, being a particularly interesting case for such future study, as well as further study of the potential for alternatives to braiding schemes for topologically protected quantum computation.

ACKNOWLEDGMENTS

We gratefully acknowledge helpful discussions with J. E. Moore, I. A. Day, and R. Calderon. This research was supported in part by the National Science Foundation under Grants No. NSF PHY-1748958 and No. PHY-2309135, and undertaken in part at Aspen Center for Physics, which is supported by National Science Foundation Grant No. PHY-2210452.

-
- [1] A. Y. Kitaev, Fault-tolerant quantum computation by anyons, *Ann. Phys.* **303**, 2 (2003).
 [2] D. Aasen, M. Hell, R. V. Mishmash, A. Higginbotham, J. Danon, M. Leijnse, T. S. Jespersen, J. A. Folk, C. M. Marcus, K. Flensberg *et al.*, Milestones toward majorana-based quantum computing, *Phys. Rev. X* **6**, 031016 (2016).

- [3] J. Alicea, Y. Oreg, G. Refael, F. Von Oppen, and M. P. A. Fisher, Non-abelian statistics and topological quantum information processing in 1D wire networks, *Nat. Phys.* **7**, 412 (2011).
 [4] C. Nayak, S. H. Simon, A. Stern, M. Freedman, and S. Das Sarma, Non-abelian anyons and topological quantum computation, *Rev. Mod. Phys.* **80**, 1083 (2008).

- [5] G. Strübi, W. Belzig, M. S. Choi, and C. Bruder, Interferometric and noise signatures of majorana fermion edge states in transport experiments, *Phys. Rev. Lett.* **107**, 136403 (2011).
- [6] B. Jäck, Y. Xie, J. Li, S. Jeon, B. A. Bernevig, and A. Yazdani, Observation of a majorana zero mode in a topologically protected edge channel, *Science* **364**, 1255 (2019).
- [7] T. Karzig, C. Knapp, R. M. Lutchyn, P. Bonderson, M. B. Hastings, C. Nayak, J. Alicea, K. Flensberg, S. Plugge, Y. Oreg *et al.*, Scalable designs for quasiparticle-poisoning-protected topological quantum computation with majorana zero modes, *Phys. Rev. B* **95**, 235305 (2017).
- [8] B. Lian, X. Q. Sun, A. Vaezi, X. L. Qi, and S. C. Zhang, Topological quantum computation based on chiral majorana fermions, *Proc. Natl. Acad. Sci. USA* **115**, 10938 (2018).
- [9] S. Plugge, A. Rasmussen, R. Egger, and K. Flensberg, Majorana box qubits, *New J. Phys.* **19**, 012001 (2017).
- [10] M. Leijnse and K. Flensberg, Parity qubits and poor man's Majorana bound states in double quantum dots, *Phys. Rev. B* **86**, 134528 (2012).
- [11] A. Calzona, N. P. Bauer, and B. Trauzettel, Holonomic implementation of CNOT gate on topological Majorana qubits, *SciPost Phys. Core* **3**, 014 (2020).
- [12] A. M. Cook and J. E. Moore, Multiplicative topological phases, *Commun. Phys.* **5**, 262 (2022).
- [13] A. Y. Kitaev, Unpaired majorana fermions in quantum wires, *Phys.-Usp.* **44**, 131 (2001).
- [14] F. Pientka, A. Keselman, E. Berg, A. Yacoby, A. Stern, and B. I. Halperin, Topological superconductivity in a planar Josephson junction, *Phys. Rev. X* **7**, 021032 (2017).
- [15] M. Hell, M. Leijnse, and K. Flensberg, Two-dimensional platform for networks of majorana bound states, *Phys. Rev. Lett.* **118**, 107701 (2017).
- [16] R. M. Lutchyn, E. P. A. M. Bakkers, L. P. Kouwenhoven, P. Krogstrup, C. M. Marcus, and Y. Oreg, Majorana zero modes in superconductor-semiconductor heterostructures, *Nat. Rev. Mater.* **3**, 52 (2018).
- [17] V. Mourik, K. Zuo, S. M. Frolov, S. R. Plissard, E. P. A. M. Bakkers, and L. P. Kouwenhoven, Signatures of Majorana fermions in hybrid superconductor-semiconductor nanowire devices, *Science* **336**, 1003 (2012).
- [18] S. Nadj-Perge, I. K. Drozdov, B. A. Bernevig, and A. Yazdani, Proposal for realizing Majorana fermions in chains of magnetic atoms on a superconductor, *Phys. Rev. B* **88**, 020407(R) (2013).
- [19] J. Alicea, Majorana fermions in a tunable semiconductor device, *Phys. Rev. B* **81**, 125318 (2010).
- [20] J. Alicea, New directions in the pursuit of Majorana fermions in solid state systems, *Rep. Prog. Phys.* **75**, 076501 (2012).
- [21] C. W. J. Beenakker, Search for Majorana fermions in superconductors, *Annu. Rev. Condens. Matter Phys.* **4**, 113 (2013).
- [22] J. D. Sau, R. M. Lutchyn, S. Tewari, and S. Das Sarma, Generic new platform for topological quantum computation using semiconductor heterostructures, *Phys. Rev. Lett.* **104**, 040502 (2010).
- [23] C. K. Chiu, J. C. Y. Teo, A. P. Schnyder, and S. Ryu, Classification of topological quantum matter with symmetries, *Rev. Mod. Phys.* **88**, 035005 (2016).
- [24] C. W. Groth, M. Wimmer, A. R. Akhmerov, and X. Waintal, Kwant: A software package for quantum transport, *New J. Phys.* **16**, 063065 (2014).
- [25] D. Varjas, T. O. Rosdahl, and A. R. Akhmerov, Qsymm: algorithmic symmetry finding and symmetric Hamiltonian generation, *New J. Phys.* **20**, 093026 (2018).
- [26] A. Alexandradinata, X. Dai, and B. A. Bernevig, Wilson-loop characterization of inversion-symmetric topological insulators, *Phys. Rev. B* **89**, 155114 (2014).
- [27] See Supplemental Material at <http://link.aps.org/supplemental/10.1103/PhysRevB.109.014516> for the relevant calculation referred to in the main text. Some extra references [33–37] are cited.
- [28] A. M. Cook and A. E. B. Nielsen, Finite-size topology, *Phys. Rev. B* **108**, 045144 (2023).
- [29] N. Leumer, M. Marganska, B. Muralidharan, and M. Grifoni, Exact eigenvectors and eigenvalues of the finite Kitaev chain and its topological properties, *J. Phys.: Condens. Matter* **32**, 445502 (2020).
- [30] N. G. Leumer, Spectral and transport signatures of 1d topological superconductors of finite size in the sub- and supra-gap regime: An analytical study, University of Regensburg, Ph.D. thesis (2021).
- [31] K. L. Zhang, P. Wang, and Z. Song, Majorana flat band edge modes of topological gapless phase in 2D Kitaev square lattice, *Sci. Rep.* **9**, 4978 (2019).
- [32] F. Schindler, A. M. Cook, M. G. Vergniory, Z. Wang, S. S. P. Parkin, B. A. Bernevig, and T. Neupert, Higher-order topological insulators, *Sci. Adv.* **4**, eaat0346 (2018).
- [33] R. D. King-Smith and D. Vanderbilt, Theory of polarization of crystalline solids, *Phys. Rev. B* **47**, 1651 (1993).
- [34] D. Vanderbilt and R. D. King-Smith, Electric polarization as a bulk quantity and its relation to surface charge, *Phys. Rev. B* **48**, 4442 (1993).
- [35] A. Alexandradinata, Z. Wang, and B. A. Bernevig, Topological insulators from group cohomology, *Phys. Rev. X* **6**, 021008 (2016).
- [36] J. K. Asbóth, L. Oroszlány, and A. Pályi, A short course on topological insulators, *Lecture Notes in Physics* (Springer Cham, 2016), Vol. 919, p. 166.
- [37] B. J. Wieder, B. Bradlyn, Z. Wang, J. Cano, Y. Kim, H. S. D. Kim, A. M. Rappe, C. L. Kane, and B. A. Bernevig, Wallpaper fermions and the nonsymmorphic dirac insulator, *Science* **361**, 246 (2018).